SAND REPORT
SAND2004-5329
Unlimited Release
Printed November 2004

Microscale Rarefied Gas Dynamics and Surface Interactions for EUVL and MEMS Applications

Daniel J. Rader, Wayne M. Trott, John R. Torczynski, Michail A. Gallis,Jaime N. Castañeda, and Thomas W. Grasser

Prepared by
Sandia National Laboratories
Albuquerque, New Mexico 87185 and Livermore, California 94550

Sandia is a multiprogram laboratory operated by Sandia Corporation, a Lockheed Martin Company, for the United States Department of Energy under Contract DE-AC04-94AL85000.

Issued by Sandia National Laboratories, operated for the United States Department of Energy by Sandia Corporation.

Available to DOE and DOE contractors from
U.S. Department of Energy
Office of Scientific and Technical Information
P.O. Box 62
Oak Ridge, TN 37831

Telephone: (865)576-8401
Facsimile: (865)576-5728
E-Mail: reports@adonis.osti.gov
Online ordering: http://www.doe.gov/bridge

Available to the public from
U.S. Department of Commerce
National Technical Information Service
5285 Port Royal Rd
Springfield, VA 22161

Telephone: (800)553-6847
Facsimile: (703)605-6900
E-Mail: orders@ntis.fedworld.gov
Online order: http://www.ntis.gov/ordering.htm

SAND2004-5329
Unlimited Release
Printed November 2004

Microscale Rarefied Gas Dynamics and Surface Interactions for EUVL and MEMS Applications

Daniel J. Rader, Wayne M. Trott, John R. Torczynski,
Michail A. Gallis, Jaime N. Castañeda, and Thomas W. Grasser
Engineering Sciences Center
Sandia National Laboratories
P. O. Box 5800
Albuquerque, New Mexico 87185-0834

Abstract

A combined experimental/modeling study was conducted to better understand the critical role of gas-surface interactions in rarefied gas flows. An experimental chamber and supporting diagnostics were designed and assembled to allow simultaneous measurements of gas heat flux and inter-plate gas density profiles in an axisymmetric, parallel-plate geometry. Measurements of gas density profiles and heat flux are made under identical conditions, eliminating an important limitation of earlier studies. The use of *in situ*, electron-beam fluorescence is demonstrated as a means to measure gas density profiles although additional work is required to improve the accuracy of this technique. Heat flux is inferred from temperature-drop measurements using precision thermistors. The system can be operated with a variety of gases (monatomic, diatomic, polyatomic, mixtures) and carefully controlled, well-characterized surfaces of different types (metals, ceramics) and conditions (smooth, rough). The measurements reported here are for 304 stainless steel plates with a standard machined surface coupled with argon, helium, and nitrogen. The resulting heat-flux and gas-density-profile data are analyzed using analytic and computational models to show that a simple Maxwell gas-surface interaction model is adequate to represent all of the observations. Based on this analysis, thermal accommodation coefficients for 304 stainless steel coupled with argon, nitrogen, and helium are determined to be 0.88, 0.80, and 0.38, respectively, with an estimated uncertainty of ±0.02.

Acknowledgment

This project, LDRD 04-1413, “Microscale Rarefied Gas Dynamics and Surface Interactions for EUVL and MEMS Applications,” was funded by the Laboratory Directed Research and Development (LDRD) program at Sandia National Laboratories. The authors thank Jeremy Barney for his support in automating our data acquisition procedures.

Table of Contents

List of Figures

List of Tables

Nomenclature

Roman Variables

$\bar{c}$	average speed of a Maxwellian distribution, $\sqrt{8k_BT/\pi m}$ [m/s]
C_p	specific heat at constant pressure [J/(kg·K)]
C_v	specific heat at constant volume [J/(kg·K)]
d	molecular hard-sphere diameter [m]
E_{in}	incident energy flux [W/m^2]
E_{re}	reflected energy flux [W/m^2]
E_w	wall-equilibrium reflected energy flux [W/m^2]
f	molecular velocity probability distribution [s^3/m^3]
g	jump coefficient [m]
K	thermal conductivity [W/(m·K)]
k_B	Boltzmann constant [1.380658×10^{-23} J/K]
L	gap between plates [m]
m	molecular mass [kg]
n	number density [1/m^3]
P	pressure [Pa]
q	heat flux magnitude [W/m^2]
T	temperature [K]
T_c	temperature of cold wall at $x = 0$ [K]
T_h	temperature of hot wall at $x = L$ [K]
T_j	jump temperature [K]
T_w	wall temperature [K]
z	Cartesian coordinate [m]

Greek Variables

α_{VSS}	VSS angular scattering parameter [1]
α	thermal accommodation coefficient [1]
γ	specific heat ratio, C_p/C_v [1]
ζ	number of internal degrees of freedom [1]
λ	mean free path, $(2\mu)/(\rho\bar{c})$ [m]
μ	absolute viscosity [Pa·s]
ρ	mass density [kg/m^3]
σ_c	total cross section divided by 4π, $d^2/4$ [m^2]
ω	VSS viscosity temperature exponent [1]
Ω	solid angle [1]

Dimensionless Variables

Kn	system Knudsen number, λ/L [1]
Pr	Prandtl number, $\mu C_p/K$ [1]

Subscripts

C	continuum
FM	free molecular
ref	reference value
wall	quantity at a solid wall boundary
c	boundary or wall at $x = 0$
h	boundary or wall at $x = L$

Acronyms

CE	Chapman-Enskog
DSMC	Direct Simulation Monte Carlo
EUVL	Extreme Ultraviolet Lithography
FS	Full Scale
IPL	Inverse Power Law
MEMS	MicroElectroMechanical Systems
VSS	Variable Soft Sphere

1. Introduction

1.1. Overview

Heat transfer to surfaces immersed in noncontinuum (transitional or rarefied) gas flow continues to be an active area of research. Gases exhibit noncontinuum effects when the characteristic length scale of the system becomes comparable to the gas mean free path. Thus, these effects become important when either the system length scale becomes small (*e.g.*, MicroElectroMechanical Systems) or when the gas pressure becomes low (*e.g.*, semiconductor manufacturing or Extreme Ultraviolet Lithography). *A priori* prediction of noncontinuum, gas-phase heat flux requires a detailed description of the gas-surface interaction. Unfortunately, and despite considerable effort over the past century, reliable gas-surface interaction mechanisms are still lacking. This gap in our understanding becomes increasingly serious as modelers are asked to perform ever more sophisticated engineering analyses of systems exhibiting marked noncontinuum behavior. It is well recognized that the remedy to this dilemma lies in the development of a reliable, experimentally-validated database of gas-surface interaction models. Ideally, this database would span the wide range of gas-surface combinations that are of interest in modern engineering applications. This LDRD-funded study has taken a major step toward meeting this need by developing an experimental chamber and diagnostics that can provide simultaneous measurements of gas heat flux and density profiles between parallel plates. This chapter explains the motivations for initiating this study and introduces the basic concepts underlying noncontinuum flow. A brief review is also provided of closely related work that has been previously reported in the literature.

1.2. Motivation

The need to predict heat transfer to a surface immersed in a noncontinuum gas is common to a variety of applications of interest at Sandia National Laboratories. Gases exhibit noncontinuum effects when the characteristic length scale of the system becomes comparable to the gas mean free path, λ, defined as the average distance traveled by a molecule between collisions. As the definition of mean free path is somewhat arbitrary, a number of definitions persist in the literature; the definition of mean free path given by Springer (1971) is used here:

$$\lambda = \frac{2\mu}{\rho \bar{c}}, \tag{1}$$

where μ and ρ are the gas viscosity and density, $\bar{c} = (8k_B T/\pi m)^{1/2}$ is the mean molecular speed, k_B is the Boltzmann constant, T is the local gas temperature, and m is the gas molecular mass. Noncontinuum effects become important when either system length scales become microscopically small or when gas pressures become low. The rise of noncontinuum behavior with decreasing pressure results from the inverse dependence of the mean free path on gas density, as given in Equation (1). Thus, at low enough pressures, even flows within/around macroscopic structures can become noncontinuum (*e.g.*, the free flight of bodies at high altitude).

Applications with microscopic length scales are becoming increasingly common since the advent of Micro Electro Mechanical Systems (MEMS), which are currently manufactured with micron-scale geometric features. Figure 1a shows a typical example: cantilevered microbeams fabricated by Sandia's SUMMiT V^{TM} process (Sniegowski and de Boer, 2000). These microbeams have a thickness of 2 μm, a width of 20 μm, a length of 100 μm, and a gap height with respect to the substrate of 2 μm. Dimensions like these are typical of microstructures, which commonly have a vertical extent of 1-10 μm and a horizontal extent of 10-1000 μm (Sniegowski and de Boer, 2000).

Microsystems are usually operated in air at ambient pressure and temperatures, for which the mean free path is ~0.065 μm (Karniadakis and Beskok, 2002). Since the mean free path is not negligibly small compared to the geometric length scales, the conduction of heat across small gas channels will exhibit noncontinuum features. Thus, engineering design tools intended for thermal management analyses in microsystems must include noncontinuum capabilities. These design tools will require specific gas-surface interaction models for the materials and finishes encountered in microsystems. This is a particularly challenging requirement, however, as most previous studies of gas-surface interactions have considered metal surfaces prepared with conventional machining methods (see Saxena and Joshi, 1989). In contrast, most microsystems are made from non-metals with nontraditional manufacturing processes (Yang and Bennett, 2000). Consequently, studies of gas interactions with non-metal surfaces are beginning to appear in the literature. Recent publications include those of Yang and Bennett (2000) who report molecular-beam measurements of thermal accommodation coefficients for nitrogen reflecting from silicon and polyimide samples, and Arkilic *et al.* (2001) who report measurements of tangential momentum accommodation in micromachined silicon channels. The recognition of the need to reliably measure thermal accommodation for typical MEMS surfaces was the primary motivation for initiating this project.

Noncontinuum gas-flow effects are also encountered when the system pressure becomes small. This approach to the noncontinuum limit arises from the fact that the mean free path is inversely proportional to the gas density; thus, at sufficiently low pressures the mean free path becomes comparable even to macroscopic length scales. One long-established field of research, rarefied gas dynamics, pertains to the study of noncontinuum flow around high-speed spacecraft in the upper atmosphere. Rarefied gas flow is also observed in low-speed, low-pressure systems, such as semiconductor and MEMS manufacturing or Extreme Ultra Violet Lithographic (EUVL) processing (see Figure 1b). Both of these applications are of particular interest to Sandia. One of the key challenges facing the development of EUVL was the protection of the lithographic mask from particle deposition. One proposed solution was the use of thermophoretic protection, in which the mask is kept slightly warmer than a parallel plate (Klebanoff and Rader, 2000; Rader *et al.*, 2002). The flow of heat from the warmer mask to the cooler plate forces particles to move away from the mask, thereby providing protection from particle contamination. A key challenge in this design is to maximize the heat flow through the gas resulting from a given temperature difference between the mask and plate. For this purpose, highly accommodating surfaces are desired. The need to measure the accommodation coefficient for various surfaces proposed for EUVL mask protection was a second motivation for this project.

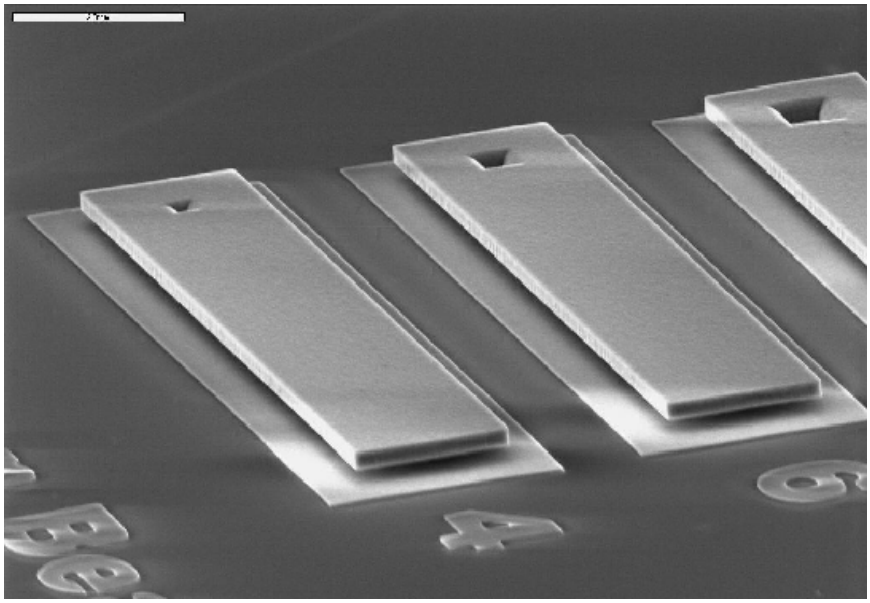

(a)

(b)

Figure 1. a) Cantilevered microbeams fabricated at Sandia using the SUMMiT V^{TM} process. b) Sandia's Extreme Ultraviolet Lithography test stand.

1.3. Gas-Surface Interactions

Momentum and heat transfer to surfaces immersed in noncontinuum gas flows continues to be the subject of many studies since Maxwell's pioneering work over 100 years ago (Maxwell, 1890). To predict momentum and heat fluxes, it is essential to know the net balance of energy and momentum carried by molecules impinging on and reflecting from a surface. Despite considerable efforts to understand this process, detailed gas-surface interaction mechanisms are still lacking (*e.g.*, Ohwada, 1996). Consequently, *a priori* prediction of rarefied flow in simple geometries continues to be an open question.

In the absence of detailed gas-surface interaction models, theoretical predictions for stress and heat transfer usually can be brought into agreement with experimental observations by using average empirical parameters called accommodation coefficients. The most widely used parameter for heat transfer is the thermal accommodation coefficient, α, which is defined by

$$\alpha = \frac{E_{in} - E_{re}}{E_{in} - E_w} \tag{2}$$

where E_{in} is the incident energy flux, E_{re} is the reflected energy flux, and E_w is the energy flux that would be achieved if the reflected molecules were emitted in thermal equilibrium at the surface temperature (Schaaf and Chambre, 1958; Springer, 1971). The thermal accommodation coefficient varies between unity (complete accommodation, diffuse reemission) and zero (specular reemission). The simple partition of gas-surface collisions into a diffuse, fully accommodated fraction and a specular fraction is often referred to as the *Maxwell wall model*, a convention which is followed in this work. Note that Equation (2) represents an average over a finite area of surface and a very large number of gas-surface collisions. Also, no attempt is made to distinguish among the possibly different accommodations for the various molecular degrees of freedom. Thus, the net flux of translational energy is lumped together with that of the rotational and vibrational modes, if present. Experimental data related to the separate contributions to the accommodation coefficient of the different energy modes are virtually nonexistent.

Previous experimental studies have measured the thermal accommodation coefficient in a variety of geometries and over a wide range of gas-surface combinations. Springer (1971) presents some typical values while an extensive review is available in Saxena and Joshi (1989). The data show that accommodation strongly depends on the composition and temperature of the gas and surface, on gas pressure, and on the state of the surface (roughness, contaminant adsorption, gas adsorption). Theoretical analyses support the same conclusions but also suggest that accommodation depends on the energy and incident angle (relative to the plane of the surface) of the incoming molecules, as well as on the reflected angle. Studies which have inferred the accommodation coefficient from bulk heat-flux measurements in a variety of geometries (*e.g.*, parallel plate or wire/tube) provide little information on the details of the reflection but are very useful for guiding engineering analyses. On the other hand, molecular beam, time-of-flight studies can provide detailed information on the angular and energy dependencies of accommodation. For example, Yang and Bennett (2000) bombarded silicon and polyimide surfaces with a well-characterized nitrogen beam and used a time-of-flight method to measure the velocity distribution

of the reflected molecules. Although these detailed studies provide valuable insight, they suffer in practice as the resulting accommodation models must be integrated over all molecular incident angles and energies. Frequently, the state of the impinging molecules is not well known.

Experimental values reported for the thermal accommodation coefficient range from 0.01 to nearly unity, depending on the gas-surface combination and the level of contaminant gas layers adsorbed on the surface. The smaller values tend to be observed for light gases striking surfaces composed of higher-atomic-weight molecules (*e.g.*, helium striking a clean tungsten surface); near unity values tend to be observed for heavy gases striking lower- or similar-molecular weight or contaminated surfaces (*e.g.*, nitrogen on silicon, xenon on tungsten). For engineering surfaces that have not been carefully cleaned, Springer (1971) suggests that the accommodation coefficient for air is between 0.8 and 0.98. Qualitative theoretical arguments predict that thermal accommodation tends to increase with increasing gas molecular weight for a given surface.

1.4. Role of Surface Accommodation in Heat Transfer

In simplest terms, the prediction of gas-phase heat conduction in a given geometry requires theoretical models characterizing molecular collisions with each other and with the walls. The combination of a Maxwell accommodation model (to describe gas-wall collisions) with gas kinetic theory (to describe molecule-molecule collisions) has been widely successful in correlating experimental heat-flux measurements in a variety of geometries. For example, the deceptively simple problem of heat transfer through a quiescent, rarefied gas between infinite parallel plates of unequal temperature has been extensively studied in the literature (for a review see Springer, 1971). The vast majority of these theoretical studies assumed a Maxwell wall model as the boundary condition and then solved the Boltzmann equation for the gas occupying the region between the walls. While most of these studies acknowledge the approximate nature of the Maxwell wall model, it is worth noting that it is the very simplicity of this model that allows for the generation of closed-form analytic solutions.

Of particular interest is the approximate four-moment solution of the linearized (for small temperature differences) Boltzmann equation given by Liu and Lees (1961) for the parallel-plate problem. Liu and Lees divided the gas molecules into two groups, each characterized by a Maxwellian velocity distribution specified by four unknown spatial functions. These unknown functions were determined by substitution into four integral moment equations. Their original work assumed complete thermal accommodation at both walls, although the analysis was later extended to arbitrary values of the accommodation coefficient (see Springer, 1971). The analysis of Liu and Lees and later extensions led to analytic expressions for the heat flux and for the gas-density profiles between the plates (for all pressures and inter-plate gaps). These analytic expressions were found to agree well with experimentally measured heat-flux and gas-density-profile data over a wide range of pressures (Teagan and Springer, 1968; Alofs *et al.*, 1971).

Despite the apparent success of the Liu and Lees method in describing experimental data, much controversy remains. Springer (1971) noted that more sophisticated mathematical solutions to the Boltzmann equation do not provide significant improvements compared to the simpler Liu and Lees formulation (and in many cases are much worse). For example, Ohwada (1996) performed a

careful finite-difference solution to the Boltzmann equation and found considerable differences between his analytical density profile results and the experimental data of Teagan and Springer; Ohwada suggested several possible weaknesses in the experiments that should be explored. Recent calculations at Sandia using the Direct Simulation Monte Carlo (DSMC) code ICARUS on the Teagan and Springer problem parallel the findings of Ohwada: a single accommodation coefficient cannot be found which will allow the model to predict both the heat flux and the inter-plate density profiles. In contrast, Wadsworth (1993) found very good agreement between his DSMC calculations and the density profile data of Alofs *et al.* (1971), using a single accommodation coefficient despite the fact the two plates used in the experiments were of dissimilar materials.

It is difficult to resolve these apparent conflicts as only two experimental studies are available which report both heat flux and density profile data in the transition regime (Teagan and Springer, 1968; Alofs *et al*. 1971). Unfortunately, neither of these two studies paid close attention to the surface condition of the plates, and neither reported heat flux and density profiles under identical conditions. Thus, a clear need exists for additional experiments. In particular, given that the gas-surface interaction is critical in understanding this rarefied gas problem, particular care must be taken in characterizing the surface state.

1.5. Goals of the Present Study

In response to the above issues, a combined experimental/modeling study was conducted to better understand the critical role of gas-surface interactions in rarefied gas flows. An experimental chamber and supporting diagnostics were developed that allow simultaneous measurements of gas heat flux and inter-plate gas density profiles in a parallel-plate geometry. Measurements of gas density profiles and heat flux can be made under identical conditions, eliminating an important limitation of earlier studies. *In situ*, electron-beam fluorescence is used to measure gas density profiles, while heat flux is inferred from temperature-drop measurements using precision thermistors. The system can be operated with a variety of gases (monatomic, diatomic, polyatomic, mixtures) and carefully controlled, well-characterized surfaces of different types (metals, ceramics) and conditions (smooth, rough). The measurements reported here are for 304 stainless steel plates with a standard milled surface coupled with argon, helium, and nitrogen. The resulting heat-flux and gas-density-profile data are analyzed using analytic and computational models to determine whether a simple Maxwell gas-surface interaction model is adequate to represent all of the observations.

2. Theory

2.1. Overview

The goal of this study is to infer gas-surface thermal accommodation coefficients from experimental measurements of the pressure-dependence of gas heat flux and gas density profiles between two parallel plates of unequal temperature. The gas-phase conduction of heat between infinite parallel plates is often referred to as the Fourier problem and has received considerable theoretical treatment in the literature because of its geometric simplicity. The following chapter reviews this theoretical literature with a particular emphasis on those results which are of use in interpreting the experimental results that will be presented later.

2.2. Fourier Geometry

The classic Fourier geometry is defined by a quiescent gas occupying the region between two infinite, parallel plates of unequal temperature. A schematic diagram of this geometry is shown in Figure 2. The two plates are separated by a gap, L, and the coordinate system is defined such that $z = 0$ corresponds to the surface of the bottom plate. The temperature of the top plate, T_h, is assumed (without loss of generality) higher than that of the lower plate, T_c. In the experiments, these two temperatures do not differ by much, so the assumption $T_h - T_c \ll T_c$ is typically satisfactory. Because of the imposed temperature difference, heat is conducted through the gas from the hot plate to the cold plate. The theoretical analyses assume that the gas is quiescent (no mass flow); consequently, the gas-phase heat transfer between the plates is dominated by conduction, and convection is neglected. Radiation is not treated theoretically in this chapter but is considered in the experimental analysis.

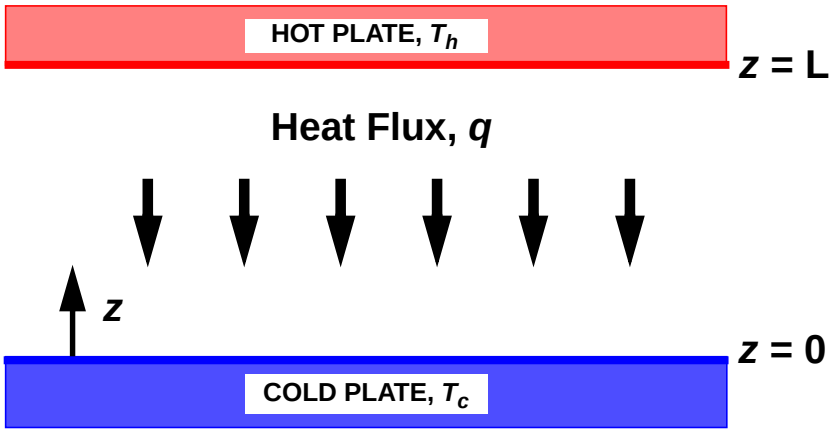

Figure 2. Schematic diagram of the Fourier heat conduction geometry.

2.3. Surface Accommodation Model

A Maxwell (1890) wall model is considered in this study. In the Maxwell model, a fraction, α, of molecules are reflected diffusely with complete thermal accommodation, while the remaining molecules, $1-\alpha$, are assumed to be reflected specularly. Molecules undergoing a diffuse reflection possess a half-range Maxwellian molecular velocity distribution in equilibrium with the wall temperature. For a specular reflection, the tangential velocity of a molecule is left unchanged while the normal velocity changes sign but not magnitude. A purely diffuse surface would be characterized by $\alpha = 1$, a purely specular surface would have $\alpha = 0$, while in the general case the surface accommodation coefficient would lie somewhere in between, $0 \le \alpha \le 1$.

As discussed in Chapter 1, the Maxwell wall model is undoubtedly overly simplistic, but it is in fact this simplicity that has made this model so popular for correlating experimental observations. In general, each wall would be expected to be characterized by a separate accommodation coefficient. Thus, α_h would be associated with the hot wall, and α_c with the cold wall. In practice, however, the experiments presented below were performed with the careful intent to maintain the materials and surface finishes of the two plates as similar as possible. In this case, the assumption is made that there is only one accommodation coefficient, $\alpha = \alpha_h = \alpha_c$.

2.4. Rarefied Gas Flow

At high enough pressures, a gas acts as a continuum and can be described by the Navier-Stokes equations. As the pressure decreases, the gas will eventually begin to exhibit noncontinuum effects, in that the discrete molecular nature of the gas becomes apparent. Manifestations of flow rarefaction include the well-known temperature-jump and velocity-slip discontinuities at walls (Springer, 1971). The onset of noncontinuum gas behavior is typically indicated by a Knudsen number, the ratio of the gas mean free path to a characteristic length of the system:

$$\mathrm{Kn} = \frac{\lambda}{L} . \tag{3}$$

For the Fourier problem, this length is taken as the plate separation, L. The gas mean free path, λ, is the average distance traveled by molecules between collisions and has been defined in Equation (1) but is repeated here for convenience:

$$\lambda = \frac{2\mu}{\rho \bar{c}},$$

where μ and ρ are the gas viscosity and density, $\bar{c}$ is the mean molecular speed,

$$\bar{c} = \sqrt{\frac{8 k_B T}{\pi m}}, \tag{4}$$

$k_B = 1.380658\times10^{-23}$ J/K is the Boltzmann constant, T is the local gas temperature, and m is the gas molecular mass.

The continuum regime is achieved when the gas mean free path is much smaller than the characteristic system length (*i.e.*, $\mathrm{Kn} \to 0$), while the free molecular (rarefied) regime is achieved when the gas mean free path is much larger than L (*i.e.*, $\mathrm{Kn} \to \infty$). A wide range of rarefied flow regime lies between these extremes. It is convenient to divide the intermediate Kn range into distinct flow regimes, and one widely accepted convention was first proposed by Schaaf and Chambre (1958): free molecular ($\mathrm{Kn} > 10$), transition ($10 > \mathrm{Kn} > 0.1$), temperature jump (slip) ($0.1 > \mathrm{Kn} > 0.01$), and continuum ($\mathrm{Kn} < 0.01$). The indicated Kn ranges are approximate only, as the nature of the flow smoothly transitions from the free molecular to the continuum regime as the Knudsen number ranges from infinity to zero. Nevertheless, these divisions are helpful in organizing the theoretical approaches to solving for the gas heat flux between plates for arbitrary levels of rarefaction.

2.5. Gas-Phase Heat Conduction

2.5.1. Free Molecular Regime (Kn > 10)

In the free molecular limit ($\mathrm{Kn} \to \infty$) molecules travel back and forth between the plates without colliding with each other; in this case the heat transfer between the plates can be described from a molecular point of view. In the free molecular limit, the space between the walls is characterized by two streams of non-collisional molecules, with higher-energy molecules streaming downward from the hot plate while lower-energy molecules stream upward from the cold plate. For a stationary gas with ζ internal degrees of freedom, Bird (1994, p. 84) has shown that the total heat flux to a surface is increased by a factor of $(1 + \zeta/4)$ compared to the translational heat flux. Thus, Bird's (1994, p. 280) monatomic-gas result for the free molecular heat flux, q_{FM}, can be extended to a polyatomic gas according to:

$$q_{FM} = -\left(\frac{8k_B}{\pi m}\right)^{1/2}\left(\frac{\alpha_h\alpha_c}{\alpha_h + \alpha_c - \alpha_h\alpha_c}\right)\left(1 + \frac{\zeta}{4}\right)(T_h^{1/2} - T_c^{1/2})P\,. \tag{5}$$

The free molecular heat flux is directly proportional to the gas pressure, P; in the limit of vanishing pressure the heat flux approaches zero, as it must in a vacuum. Some simplification of Equation (5) is possible for the present experimental case where the wall accommodation coefficients are assumed equal and the temperature difference between the walls is small:

$$\boxed{q_{FM} = -\frac{1}{2}\left(\frac{P\bar{c}}{T}\right)\left(\frac{\alpha}{2-\alpha}\right)\left(1 + \frac{\zeta}{4}\right)(T_h - T_c)\,, \qquad \begin{matrix}\alpha_h = \alpha_c = \alpha \\ T_h - T_c \ll T_c\end{matrix}\quad,} \tag{6}$$

where $T = T_h^{1/2}T_c^{1/2}$ and the approximation $T_h^{1/2} + T_c^{1/2} \approx 2T^{1/2}$ has been used. No gradients in macroscopic gas properties are observed in the free molecular limit. In particular, the temperature is constant across the domain with a value equal to the geometric mean of the two wall temperatures, $T = T_h^{1/2}T_c^{1/2}$. Note that for small temperature differences between the plates, the geometric mean is closely approximated by the average temperature. Gas pressure is also constant in the region between the plates.

2.5.2. Continuum Regime (Kn < 0.01)

For small system Knudsen numbers (Kn $\rightarrow$ 0), a gas acts as a continuum, and the solution to the energy equation is found using the well-known Fourier heat conduction law. In this case, the continuum heat flux, q_C, is given by

$$q_C = -K(T)\frac{dT}{dz}, \tag{7}$$

where K is the gas thermal conductivity which depends on temperature. Equation (7) applies equally well for any gas (*i.e.*, monatomic, diatomic) if the appropriate value of K is used. The one-dimensional nature of the Fourier geometry requires that the heat flux be constant across the domain (independent of z). Note that the thermal conductivity is independent of pressure; hence, the heat flux is also independent of pressure as long as the flow lies in the continuum regime.

Equation (7) can be solved analytically for certain choices of the temperature-dependence of the thermal conductivity. One such choice is for a Variable Soft Sphere (VSS) molecular-interaction model, which leads to power-law temperature dependencies of the coefficient of viscosity and the thermal conductivity (Bird, 1994, p. 68):

$$\mu = \mu_{\text{ref}}\left(\frac{T}{T_{\text{ref}}}\right)^{\omega} \tag{8}$$

$$K = K_{\text{ref}}\left(\frac{T}{T_{\text{ref}}}\right)^{\omega}. \tag{9}$$

Experimental data are used to specify the reference viscosity, μ_{ref}, and reference conductivity, K_{ref}, at reference temperature, T_{ref}. The temperature exponent ω results from a best fit of experimental viscosity data near the reference temperature. Reference values for the transport coefficients and the temperature exponent are given in a later section. Given a power-law temperature dependence of the thermal conductivity, Equation (7) can be solved to give the following nonlinear expression for the one-dimensional heat flux:

$$q_C = -\frac{K_{\text{ref}}\left(T_h^{\omega+1} - T_c^{\omega+1}\right)}{(\omega+1)T_{\text{ref}}^{\omega} L}. \tag{10}$$

For small temperature variations, the thermal conductivity can be assumed constant, and Equation (7) can be integrated to obtain:

$$\boxed{q_C = -K\frac{T_h - T_c}{L}, \qquad T_h - T_c \ll T_c} \tag{11}$$

Note that Equation (11) can also be obtained from Equation (10) in the limit $\omega \rightarrow 0$.

2.5.3. Temperature Jump Regime (0.01 < Kn < 0.1)

As the Knudsen number increases from zero, the continuum assumption begins to break down. Rarefaction effects first become apparent at the walls in the form of temperature discontinuities, often referred to as temperature jumps. To illustrate, a schematic diagram showing three hypothetical temperature profiles is shown in Figure 3 for plates held at T_c = 263 and T_h = 283 K and separated by a 1 mm gap. In the continuum limit (Kn $\rightarrow$ 0), the gas temperature at each wall equals the wall temperature, and the profile is linear in the interior as predicted by Equation (11). Also shown is a free molecular (Kn $\rightarrow \infty$) temperature profile, which is constant at the geometric mean temperature (which is displaced slightly below the mean temperature). For intermediate Knudsen numbers, the temperature profile lies between these two limiting profiles. Similar to the continuum limit, the intermediate-Kn profile is nearly linear over most of the interior of the domain; in this region the heat flux can be described using the continuum result, Equation (7), with the local temperature gradient and the continuum thermal conductivity. Noncontinuum effects are localized in regions near the walls, known as the Knudsen layers, where departures from the interior, linear profile are clearly observed. Also evident are the discontinuities in temperature between the wall and the adjacent gas. Near the hot wall, the temperature of the adjacent gas is cooler than the wall, while near the cold wall the adjacent gas is warmer. The magnitude of the temperature jump was first given by Smoluchowski (Kennard, 1938), who gave an expression relating the wall temperature, T_{wall}, and the temperature, T_j, that the gas would have if the interior gas-temperature profile were extrapolated to the wall:

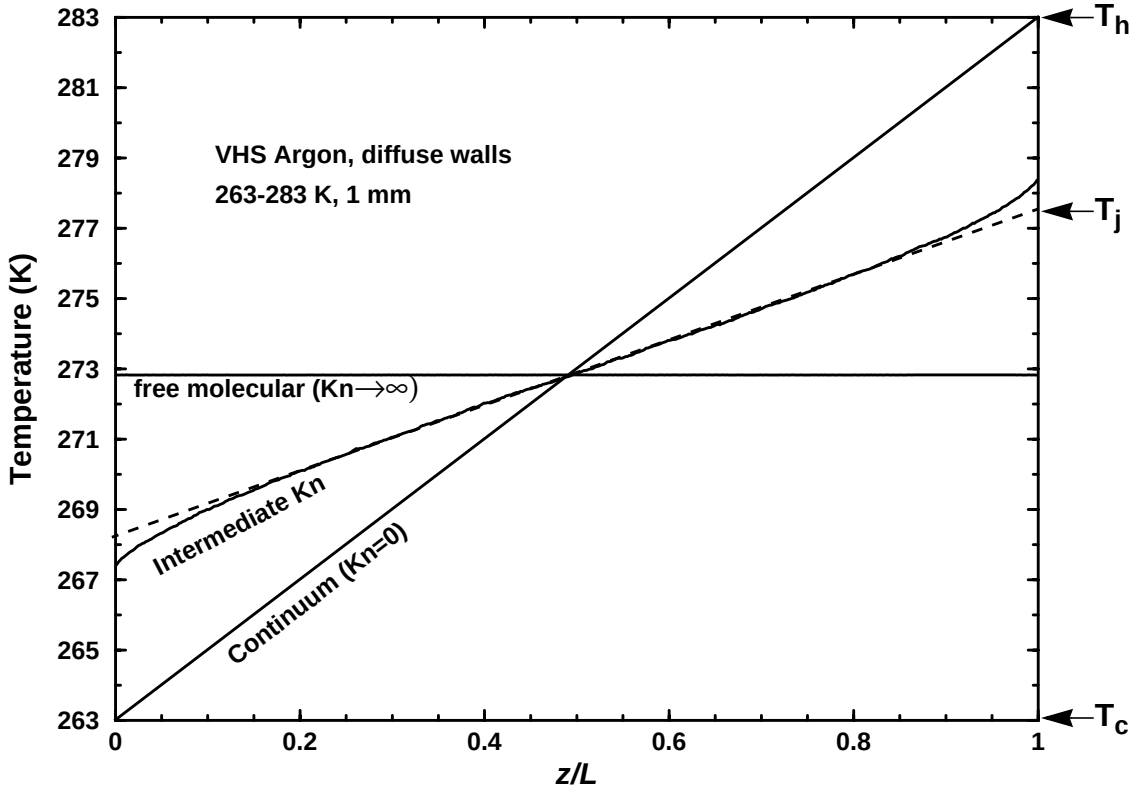

Figure 3. Schematic diagram of several temperature profiles.

$$(T_j - T_{\text{wall}}) = g\frac{dT}{dz}$$
$$g = \left(\frac{2\gamma}{\gamma+1}\right)\left(\frac{2-\alpha}{\alpha}\right)\frac{\lambda}{\text{Pr}} \tag{12}$$

where $\gamma = C_p/C_v$ is the ratio of specific heats and the Prandtl number is given by

$$\text{Pr} = \frac{\mu c_p}{K}. \tag{13}$$

Equation (12) is valid when the temperature jump is not too large. Solving Equation (7) with the jump conditions at each wall given by Equation (12) (after Kennard, 1938), an expression for the heat flux in the temperature-jump regime, q_{TJ}, can be given as:

$$\frac{q_{TJ}}{q_C} = \frac{1}{1+(2g/L)} \qquad \begin{matrix}\alpha_h = \alpha_c = \alpha \\ T_h - T_c \ll T_c\end{matrix} \tag{14}$$

where the small-temperature and equal-accommodation restrictions are explicitly noted. Under these restrictions, the definition of the jump coefficient, *g*, can be combined with the small-temperature limits for continuum and free molecular heat flux to obtain

$$g = \frac{L}{2}\frac{q_C}{q_{FM}}. \tag{15}$$

Consequently, Equation (14) can be rewritten in the simple form:

$$\frac{q_{TJ}}{q_C} = \frac{1}{1+\dfrac{q_C}{q_{FM}}} \qquad \begin{matrix}\alpha_h = \alpha_c = \alpha \\ T_h - T_c \ll T_c\end{matrix} \quad . \tag{16}$$

where the free molecular and continuum heat fluxes are given by Equations (6) and (11), respectively.

2.5.4. Transition Regime (0.1 < Kn < 10)

The prediction of the heat flux in the gas transition region is challenging, ultimately requiring a complete solution of the Boltzmann equation. Although many theoretical analyses are available in the literature (for a review, see Springer, 1971), few result in closed-form expressions for the heat flux. One exception is the analysis of Liu and Lees (1961), who used a four-moment solution of the linearized Boltzmann equation for a monatomic gas to derive an approximate, closed-form expression for the heat flux that is valid for all Kn. Interestingly, the expression derived by Liu and Lees is identical to the temperature-jump result given above, Equation (16). Springer (1971)

extended Liu and Lees' analysis to polyatomic gases and presented the following expression for the heat flux, q, which is intended to apply over the entire Kn range:

$$\frac{q}{q_C} = \frac{1}{1+\dfrac{q_C}{q_{FM}}} = \frac{1}{1+\dfrac{2KT}{L\left(\dfrac{\alpha}{2-\alpha}\right)\left(1+\dfrac{\zeta}{4}\right)\bar{c}P}} \qquad \begin{matrix}\alpha_h = \alpha_c = \alpha \\ T_h - T_c \ll T_c\end{matrix} \tag{17}$$

where $\bar{c} = (8k_BT/\pi m)^{1/2}$. Springer (1971) has shown that Equation (17) agrees reasonably well with the limited available experimental data for monatomic and diatomic gases over a wide range of Knudsen numbers. Interestingly, Springer notes that ostensibly more accurate solutions to the Boltzmann equation (*e.g.*, eight-moment methods) typically show poorer agreement with data than the simpler Liu and Lees four-moment solution. Independently, Sherman (1963) suggested a simple interpolation formula for heat flux that has the same form as Equation (17), except that he allowed the continuum and free molecular heat fluxes to be calculated from their complete (not linearized) expressions, such as Equations (5) and (10). For convenience, we will often refer to Equation (17) as the "Sherman-Lees" interpolation formula for heat flux.

Several theoretical plots of the dependence of heat flux on pressure for argon are shown in Figure (4). The cold and hot walls are held at 5 and 45°C, respectively, and are separated by 10 mm. Complete accommodation is assumed: $\alpha = 1$. The continuum and free molecular limits are shown as dotted lines. The free molecular heat flux exhibits a linear dependence on pressure, while the continuum heat flux is independent of pressure. The Sherman-Lees interpolation formula is also plotted and shows a smooth transition between the two limiting cases. Also shown are several points calculated by the Direct Simulation Monte Carlo (DSMC) method which will be discussed in Chapter 4. These numerical simulations assumed a Maxwell wall model with complete accommodation. The agreement with the Sherman-Lees interpolation is reasonably good although the DSMC calculations fall ~8% below the interpolation for intermediate pressures (~20 mTorr).

For analysis of the experimental data to be presented later, it is convenient to rewrite Equation (17) in the following form:

$$\frac{1}{q} = \frac{1}{q_C} + \frac{1}{q_C}\cdot\frac{2KT}{L\left(\dfrac{\alpha}{2-\alpha}\right)\left(1+\dfrac{\zeta}{4}\right)\bar{c}}\cdot\frac{1}{P}. \tag{18}$$

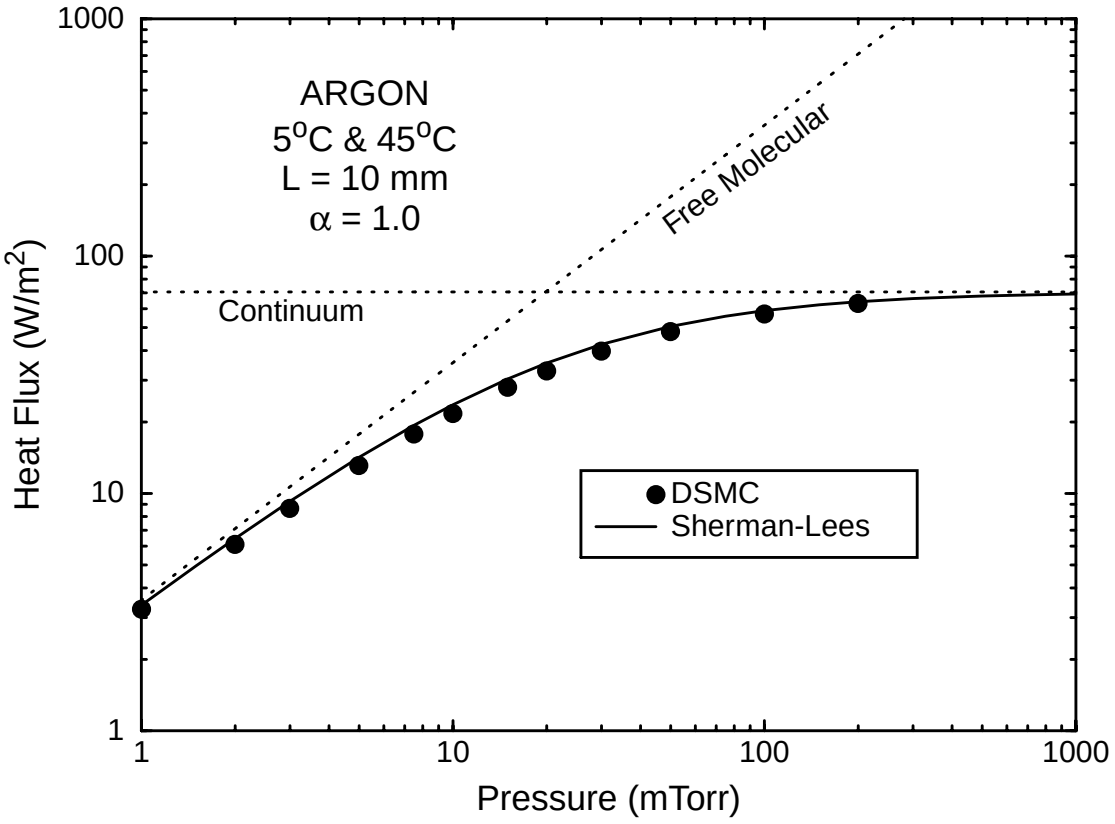

Figure 4. Theoretical predictions of heat flux vs. pressure for argon.

3. Gas Properties

Because many of the experimental results presented below are normalized by the continuum-limit heat flux, it is essential to use the most accurate values for molecular physical properties and the transport coefficients. Consequently, a brief literature search was conducted to determine the best-available properties for the three gases of interest in this report: argon, helium, and nitrogen. The temperature range of interest in this study is $0°C < T < 100°C$ (because of the use of water baths for temperature control), and the experiments are typically conducted with the plate temperatures symmetric about 298.15 K. Thus, the reference temperature for this study is taken as $T_{ref} = 298.15$ K and transport properties are tabulated over the range $273 \text{ K} < T < 380 \text{ K}$.

For monatomic gases, several authors (Hurly and Moldover, 2000; Aziz *et al.*, 1995; Bich *et al.*, 1990) have suggested that the most accurate estimates of the transport properties of monatomic gases can be obtained based on kinetic-theory calculations using accurate *ab initio* interatomic potentials. These potential-based theoretical values are found to agree with the most reliable experimental data to within reported experimental accuracies (Hurly and Moldover, 2000; Aziz *et al.*, 1995; Bich *et al*., 1990). Bich *et al.* (1990) provide tables of the viscosity and thermal conductivity of the monatomic gases based on kinetic-theory (Chapman-Enskog) calculations of the transport properties using accurate HFD-B type interatomic potentials. Their tabulations provide the temperature dependence of these transport properties in both the zero-density limit and at one atmosphere. For our present experiments at pressures well below ambient, the zero-density limit is closely approached and these are the data reported in the tables below. Bich *et al*. (1990) estimate the relative uncertainties of their recommended transport values to be 0.3% at 298.15 K, and 0.5% over the present range of interest (0-100°C). Aziz *et al.* (1995) suggest that their *ab initio* results for helium are more accurate than the best available measurements and should be used to calibrate measuring apparatus. For this purpose, they report values at 298.15 K (25°C) of $K = 154.81 \pm 0.08$ mW/(m·K) and $\eta = 19.800 \pm 0.010$ μPa·s. More recently, Hurly and Moldover (2000) also claim that the uncertainties in their tabulated, *ab initio* values of the thermophysical properties of helium are smaller than the corresponding experimental uncertainties.

In this work the tabulated values of Bich *et al*. (1990) have been accepted for monatomic gases (argon and helium) and are summarized in Table (1). Although Aziz *et al*. (1995) claim better accuracy, they only report values at one temperature. The viscosity and conductivity values of the two groups agree to within 0.20% and 0.12%, respectively, which is within the stated uncertainty of Bich *et al*. (1990). The tabulated values for helium reported by Hurly and Moldover (2000) are also in excellent agreement (within 0.15%) with the Bich *et al.* values.

For nitrogen, the transport properties tabulated by Stephan *et al.* (1987) are used based on a critical evaluation of the available experimental literature. Their viscosity values agree with their carefully screened experimental database with an average deviation of 0.11% and a standard deviation of 0.33%; their conductivity values agree with experimental data with an average deviation of -0.01% and a standard deviation of 0.77%. Stephan's viscosity values agree well with other values reported in the literature.

Table 1. Gas Transport Properties[a]

	Argon[b]		Helium[b]		Nitrogen[c]	
T (K)	μ μPa·s	*K* W/(m·K)	μ μPa·s	*K* W/(m·K)	μ μPa·s	*K* W/(m·K)
273.15	20.98	0.01638	18.69	0.1460	(16.64)	(0.02417)
280	21.43	0.01674	19.01	0.1485	16.96	0.02465
290	22.07	0.01724	19.47	0.1521	17.44	0.02533
298.15	22.59	0.01765	19.84	0.1550	(17.81)	(0.02588)
300	22.71	0.01774	19.92	0.1557	17.90	0.02601
320	23.96	0.01872	20.82	0.1627	18.80	0.02733
340	25.18	0.01968	21.70	0.1696	19.69	0.02863
360	26.37	0.02061	22.57	0.1764	20.54	0.02989
380	27.53	0.02152	23.43	0.1831	21.38	0.03113

a. Table values included in parenthesis (-) are interpolated from the reported values.
b. Bich *et al.* (1990)
c. Stephan *et al*. (1987)

Numerical simulations of the Fourier problem were performed for this study using the Direct Simulation Monte Carlo (DMSC) method, which is described below. DSMC calculations require a reference viscosity at a reference temperature: these are taken from Table (1). The method also requires molecular mass, an angular collision parameter, α_{VSS}, and the viscosity temperature exponent, ω: these values are listed in Table (2). The parameter ω was determined from a best-fit regression of the viscosity values in the range of experimental interest, $0°\mathrm{C} < T < 100°\mathrm{C}$. Calculations of viscosity and thermal conductivity using the best-fit values for ω in Equations (8) and (9) match the tabulated gas data to within 0.3%. The parameters used in this study differ somewhat from the values typically preferred by the DSMC community (*i.e.*, Bird, 1994), which probably represent a much larger temperature range, so Bird's parameters are therefore not as accurate in the restricted temperature range of interest in this study.

Table 2. Physical Properties and Parameters for DSMC.

Gas	Mass, *m* (kg)	ω	α_{VSS}	μ_∞/μ_1	K_∞/K_1
Argon	6.634×10^{-26}	0.830	1.40	1.001822	1.002862
Helium	6.647×10^{-27}	0.684	1.26	1.006330	1.009951
Nitrogen	4.652×10^{-26}	0.770	1.36	1.003342	1.005249

4. Direct Simulation Monte Carlo (DSMC) Method

4.1. Overview

Numerical simulations of the rarefied Fourier problem were performed to help guide the experiments and to interpret the resulting data. In order to capture the noncontinuum aspects of the problem, the Direct Simulation Monte Carlo (DSMC) method was used. DSMC is a well-established, molecular-based method for solving noncontinuum gas flows. Developed by Bird and discussed extensively in monographs and review articles (Bird, 1970, 1976, 1978, 1994), DSMC provides approximate solutions to the Boltzmann equation. This chapter briefly reviews the DSMC method and describes the present implementation.

4.2. The Boltzmann Equation

The Boltzmann equation describes the behavior of a noncontinuum gas under the following conditions (Gombosi, 1994): 1) the gas is dilute (only binary molecular collisions are considered), 2) "molecular chaos" applies (the states of any two colliding molecules are uncorrelated), 3) the molecules possess spherically symmetric interaction potentials, 4) classical mechanics applies (relativistic and quantum effects are neglected), 5) the extent of the intermolecular potential is small compared to other length scales (*i.e.*, the intermolecular separation, mean free path, and gradients of statistical quantities), and 6) external forces are neglected. Under these assumptions, the Boltzmann equation for the molecular velocity distribution function for a single-species monatomic gas is given by (Bird, 1976, 1994):

$$\frac{\partial F}{\partial t} + \mathbf{u} \cdot \frac{\partial F}{\partial \mathbf{x}} + \mathbf{a} \cdot \frac{\partial F}{\partial \mathbf{u}} = \int_{-\infty}^{\infty} \int_{0}^{4\pi} (F[\mathbf{v}']F[\mathbf{u}'] - F[\mathbf{v}]F[\mathbf{u}]) |\mathbf{v} - \mathbf{u}| \sigma_c d\Omega d\mathbf{v}, \tag{19}$$

$$F = nf, \int f[\mathbf{u}] d\mathbf{u} = 1. \tag{20}$$

Here, $F d\mathbf{x} d\mathbf{u}$ is the number of molecules at time t with positions within $d\mathbf{x}$ around $\mathbf{x}$ and velocities within $d\mathbf{u}$ around $\mathbf{u}$, and f is the corresponding probability density in velocity space. The quantity $\mathbf{a}$ on the left side of the equation is the body force per unit mass (*i.e.*, acceleration), here taken to be independent of the molecular velocity $\mathbf{u}$. The term on the right side of the equation is the collision integral, where the unprimed and primed quantities refer to the precollision and postcollision velocities, respectively. The quantity $\sigma_c d\Omega$ is the differential cross section for collisions, where, for elastic hard-sphere (HS) molecules of diameter d, the quantity σ_c has a value of $d^2/4$ (Bird, 1976). Generalization to gases with multiple monatomic species is straightforward; however, generalization to molecules with internal energy is more difficult.

Macroscopic quantities are determined from the Boltzmann equation by computing the corresponding moments of the molecular velocity distribution. For example, the average number density and velocity are given by the following moments.

$$n = \int_{-\infty}^{\infty} F[\mathbf{u}]d\mathbf{u}, \tag{21}$$

$$\langle \mathbf{u} \rangle = \int_{-\infty}^{\infty} \mathbf{u} f[\mathbf{u}]d\mathbf{u} = \frac{1}{n}\int_{-\infty}^{\infty} \mathbf{u} F[\mathbf{u}]d\mathbf{u}. \tag{22}$$

Closed-form analytical solutions of the Boltzmann equation are known for only a few situations. Solutions in the continuum nonequilibrium regime are provided by Chapman-Enskog theory (Chapman and Cowling, 1970). This approach involves a Taylor-series expansion that relies on the smallness of the mean free path compared to length scales associated with gradients of macroscopic quantities like temperature. Important successes of Chapman-Enskog theory include the derivation of the Newtonian and Fourier constitutive relations for shear stress and heat flux, the determination of the values of the associated transport coefficients, and the prediction of noncontinuum gas effects like thermal diffusion in gas mixtures (Chapman and Cowling, 1970). Thus, in the continuum nonequilibrium limit, the Boltzmann equation reduces to the Navier Stokes equations.

4.3. DSMC Procedure

The DSMC method uses computational molecules to provide an approximate solution to the Boltzmann equation (Bird, 1994). Each computational molecule typically represents a large number of real molecules and undergoes the same types of processes during a time step that real molecules experience: movement from one location to another, interaction with boundaries, and collision with other molecules. Computational molecules move in a ballistic fashion, traveling at constant velocity along straight-line trajectories during a time step. Following movement, boundary conditions are applied. In the case of a solid surface, a computational molecule crossing this boundary is reflected back into the domain by finding the crossing point, assigning a new velocity to the computational molecule, and allowing it to move from this point at the new velocity for the remainder of the time step. The reflected velocity assigned to the computational molecule is selected stochastically from a prescribed distribution. In this study, the Maxwell wall model is assumed and a fraction α of the molecules are reflected diffusely with perfect accommodation, while the remainder undergo a specular reflection. Following movement and reflection from boundaries, computational molecules are allowed to collide in a binary fashion. Pairs of molecules are selected randomly at the appropriate rate and are allowed to collide, by which it is meant that they are assigned postcollision velocities and internal energies (but not new positions). These postcollision values conserve mass, momentum, and energy and are selected stochastically so as to maintain the prescribed collision statistics, which determine important macroscopic properties like the temperature dependence of the transport coefficients.

The Variable Soft Sphere (VSS) model is typically used to specify postcollision velocities (Bird, 1994). The VSS model requires four parameters per collision: the reference temperature T_{ref}, the reference diameter d_{ref}, the viscosity temperature exponent ω, and the angular scattering parameter α_{VSS}. The viscosity temperature exponent usually lies in the range $1/2 \le \omega \le 1$ and produces a temperature dependence for the viscosity, thermal conductivity, and self-diffusion coefficient of $(T/T_{\text{ref}})^{\omega}$. The values $\omega = 1/2$ and $\alpha_{VSS} = 1$ correspond to hard-sphere molecules, and the values $\omega = 1$ and $\alpha_{VSS} = 2.139862$ correspond to Maxwell molecules. For general inverse-power-law (IPL) molecules in which the intermolecular force varies inversely with the intermolecular separation to the power ν, the VSS parameters can be used to calculate the reference diameter (Torczynski et al., 2003; Gallis et al., 2004):

$$d_{\text{ref}} = \left(\frac{5(\alpha + 1)(\alpha + 2)(m k_B T_{\text{ref}}/\pi)^{1/2}}{4\alpha(5 - 2\omega)(7 - 2\omega)(\mu_1/\mu_\infty)\mu_{\text{ref}}} \right)^{1/2} , \tag{23}$$

Here, the subscript “ref” denotes a quantity at the reference temperature and μ_∞/μ_1 denotes the ratio of the infinite-approximation and first-approximation values from Chapman-Enskog (CE) theory (Chapman and Cowling, 1970; Torczynski et al., 2003; Gallis et al., 2004). The temperature exponent ω is found as the best-fit to experimental viscosity data (see previous chapter), and α_{VSS} is taken from Bird (1994, Appendix A). These values are listed in Table 2 of the previous chapter, along with the values for μ_∞/μ_1. Reference viscosities at the reference temperature $T_{\text{ref}} = 298.15$ K are given in Table 1.

The computational mesh in a DSMC simulation performs two functions. First, computational molecules must be in the same mesh cell in order to collide with each other. Second, the computational mesh is used to accumulate moments of the molecular velocity distribution, such as the number density and the velocity. These molecular properties are sampled before and after the collisions are performed. Although conserved moments such as momentum are unchanged by collisions, higher-order moments such as shear stress and heat flux can be significantly affected. The above double-sample strategy significantly improves the accuracy of these quantities (Gallis et al., 2004). The uncertainties in the moments that result from molecular fluctuations can be reduced by sampling many computational molecules. For a stationary (statistically steady) flow, the ergodic hypothesis is employed: large numbers of molecules are sampled by averaging over large numbers of time steps. For an unsteady flow, either large numbers of molecules per cell must be used, or an ensemble of many simulations must be sampled, where each simulation takes a different path through phase space (usually by starting with a different random seed).

The accuracy of a DSMC simulation is governed by the choice of the mesh cell size, the time step, and the average number of molecules per cell. Reasonable accuracy is obtained when the cell size is one third or less of a mean free path, the time step is one third or less of the time required by molecules to cross a cell, and the number of computational molecules per cell exceeds about 30 (Bird, 1994). Theoretical investigations have led to a rigorous proof that, as the numerical parameters approach their limits, DSMC converges to a solution of the Boltzmann equation (Wagner, 1992).

5. Experimental Apparatus

5.1. Overview

This chapter describes the design and operation of the vacuum test chamber, all supporting hardware subsystems, and the diagnostics. The vacuum test chamber was specifically designed to accommodate all of the control systems and diagnostics needed to provide simultaneous heat-flux and gas-density-profile measurements between two parallel, 14.25-cm-diameter plates. Heat flux between the plates was inferred from temperature-drop measurements between precision thermistors embedded near the exposed surface of each plate and those immersed in an adjacent water plenum. Gas-density profiles were inferred from the fluorescence intensity of the gas illuminated with a tightly-collimated electron beam. Two particularly challenging design requirements that were met were to provide pressure isolation between the electron gun and the main chamber and to provide two temperature-controlled, movable plate assemblies. The high degree of accuracy required for this project placed severe requirements on control and measurement subsystems. Consequently, state-of-the-art components were selected for controlling system pressure, flow rate, plate alignment, plate temperatures, and plate positions. High-precision, high-accuracy, state-of-the-art components were selected for measuring system pressure, temperature, and fluorescence intensity. The present test chamber and supporting subsystems represent a significant investment in staff time, materials, and equipment.

5.2. Vacuum Test Chamber

The vacuum test chamber was specifically designed to accommodate all of the control systems and diagnostics needed to provide simultaneous heat-flux and gas-density-profile measurements. The test chamber meets two additional, challenging requirements: 1) provide pressure isolation between the electron gun (e-gun) and the main chamber, and 2) provide two independent, temperature-controlled, movable plate assemblies. The isolation requirement arose because of the need to operate the e-gun at a pressure below $\sim 1 \times 10^{-6}$ Torr. The requirements on the plate assemblies arose because of the critical role the plate temperatures, alignment, and inter-plate gap play in determining the heat flux. The test chamber and these key subassemblies were designed as an integral unit with a commercial CAD package (Solid Works); shop drawings generated by this package were provided to machine shops for fabrication. A schematic of the final chamber design (including the plate and e-gun isolation assemblies) is shown in cross-section in Figure 5. The test chamber is a 41-cm sphere with six 33.66-cm (13.25-in) OD standard conflat flanges welded as shown. The opposing upper and lower flanges were used to mount the upper and lower plate assemblies. The e-gun isolation assembly was mounted on the left-side flange (as drawn); a Faraday cup and various system diagnostics were mounted on a diagnostic plate that occupied the opposed (right-side) flange. An observation window (optical-quality quartz) occupied the flange extending out of the plane in Figure 5. The flange opposite the observation window was used to provide access for a cryogenic pump that could be isolated from the chamber by a pneumatic gate valve. A photograph of the test chamber and associated support systems is shown in Figure 6. The various control and measurement systems attached to the test chamber are each discussed below.

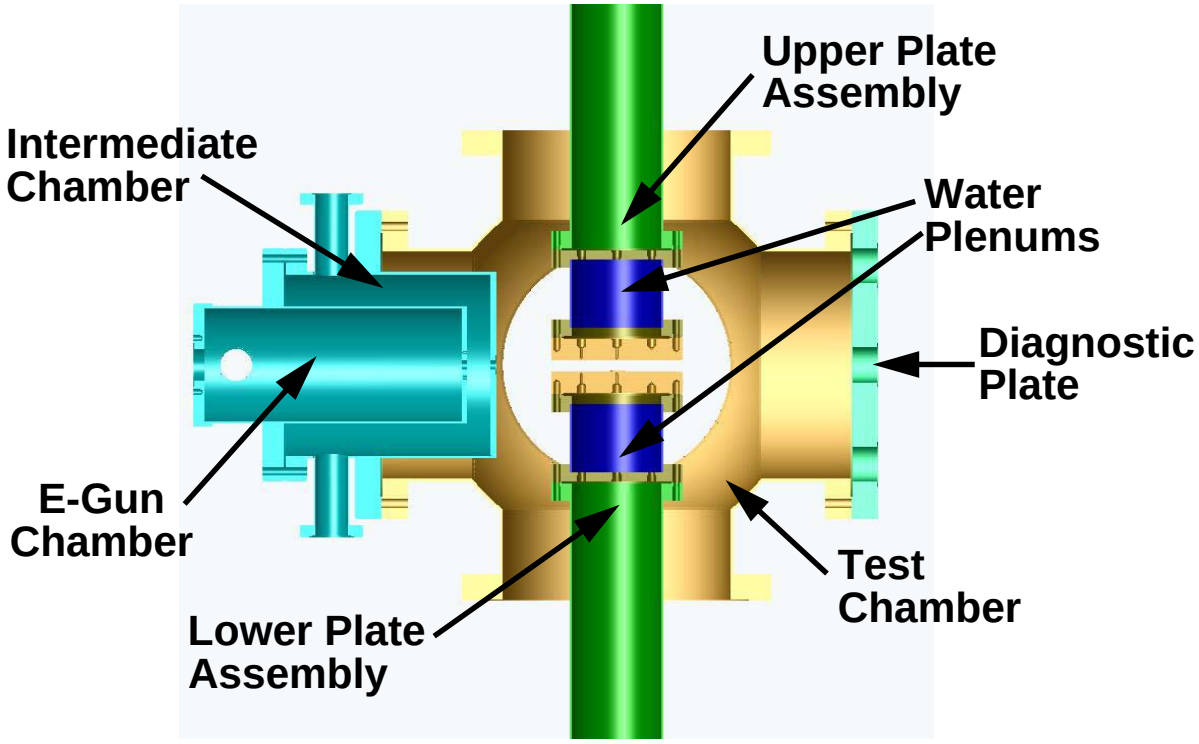

Figure 5. Schematic diagram of the test-chamber

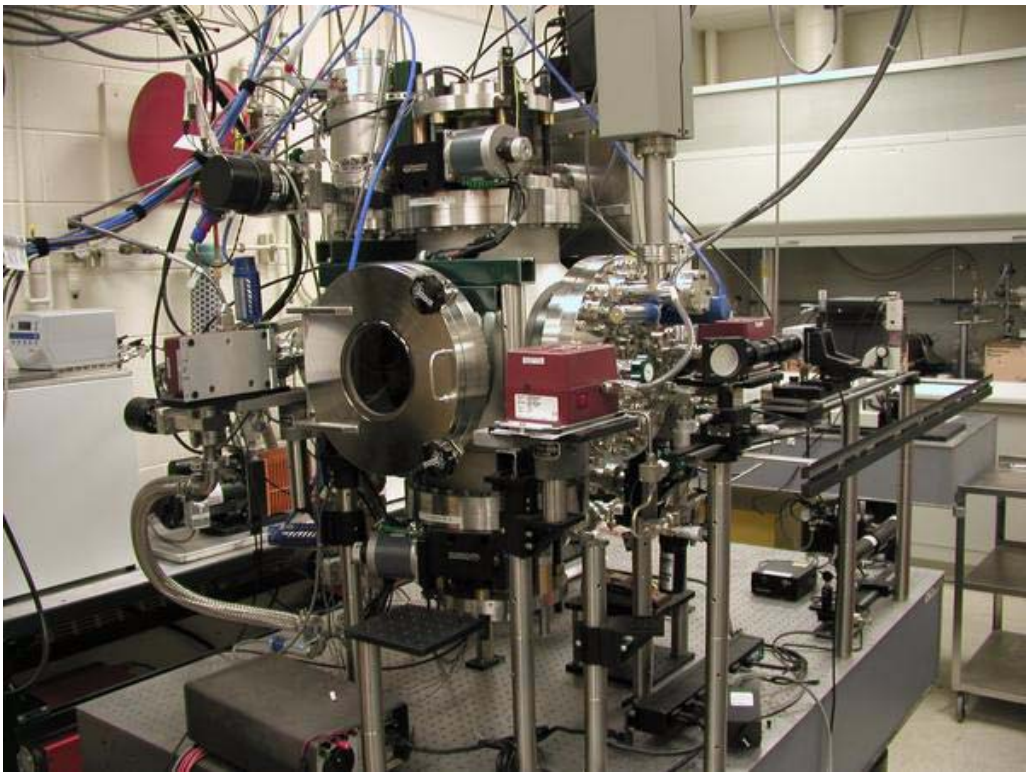

Figure 6. Front view of assembled test chamber (observation window in foreground).

5.3. Electron Gun and Pressure Isolation Assembly

Gas-density profiles between the plates are inferred from the fluorescence intensity of molecules illuminated by a tightly-collimated e-beam. The principle of operation is that when a gas is bombarded with electrons, a fraction of molecules are excited. When these excited molecules return to their ground state, they emit photons at a quantum-specified wavelength. With careful selection of emission lines (Gochberg, 1997), the intensity of the net fluorescence emission is proportional to the density of the gas in the illuminated region. E-beam fluorescence provides a single diagnostic that will work with a wide range of gases and their mixtures. With calibration, the method can be used over a wide range of gas densities. The electron beam source is a Model EMG-12 Electron Gun obtained from Kimball Physics, Inc. This device is equipped with a LaB_6 cathode (small-spot option) that can generate a focused beam waist < 200 μm in diameter at a working distance of 200 mm or more. The gun can be operated over an energy range of 500 eV to 20 keV and can generate beam currents up to 100 μA. Beam stability is specified as ±1.0% per hour when operated in Emission Current Control mode.

Operation of the electron gun (with the LaB_6 cathode) is not recommended at pressures greater than 10^{-6} Torr. On the other hand, main-chamber pressures above 1 Torr are needed for the experiments. To satisfy these conflicting requirements, we designed a dual-chamber, dual-pumped assembly that attaches to a main chamber flange. This pressure-isolation assembly is shown in Figure 5 mounted to the left-side chamber flange. The final design used two 970-μm pin-hole orifices to isolate three pressure regions (test chamber, intermediate chamber, and e-beam source chamber) and enable differential pumping. This design provides the required pressure isolation while allowing the e-beam to propagate from the source, through the pin-hole orifices, and into the test chamber. Cryogenic pumps are installed on the e-gun source and main chambers, while a turbo pump is installed on the intermediate chamber where the most pumping speed is needed. With 970-μm-diameter pinholes and nitrogen as the test gas, the e-gun chamber can be maintained at $< 5 \times 10^{-7}$ Torr while the pressure in main vacuum chamber is held at 30 mTorr.

Alignment of the two pin holes with the e-beam axis proved exceptionally challenging and was accomplished with a high-magnification, long-working-distance optical imaging system. Stray magnetic fields caused considerable beam steering and made alignment impossible until the interior of the e-gun chamber was lined with μ-metal shielding (which is highly impermeable to magnetic fields). A Faraday cup located on the diagnostics plate opposite the e-gun provides a measurement of e-beam intensity after traversing the chamber and also serves as an e-beam dump.

5.4. Flow and Pressure Measurement and Control

The stable control and accurate measurement of gas conditions in the test chamber are essential prerequisites for making the measurements desired in this project. Of particular importance is the system pressure, which must be stably maintained at a user-selected value that is accurately known. This requirement is complicated by the fact that, during testing, a flow of gas must be admitted to the chamber to replace that pumped out through the e-gun pin-hole orifice. The

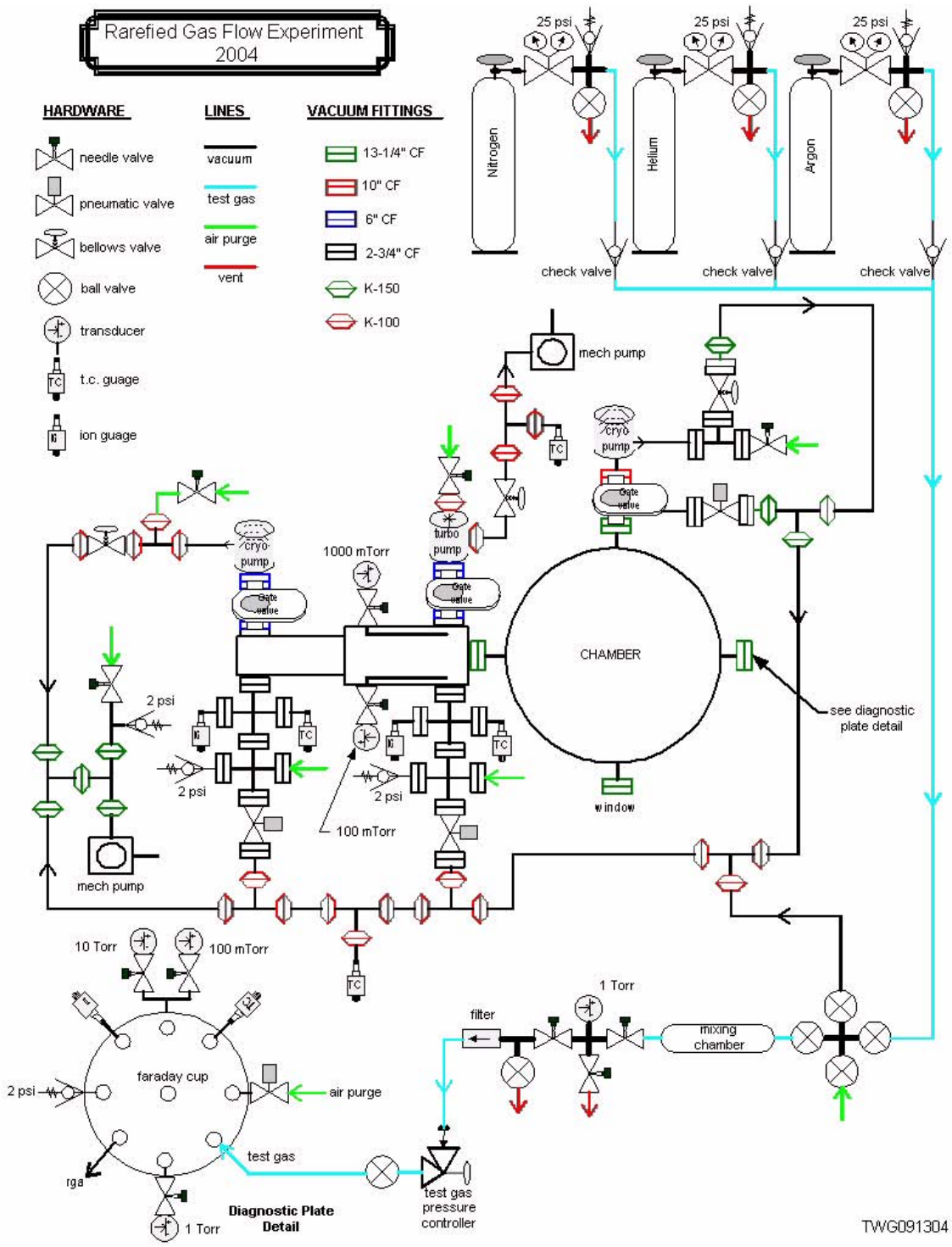

Figure 7. Schematic diagram of flow and pressure measurement and control systems.

solution was to actively regulate gas flow into the chamber based on a comparison between the measured pressure and an operator-selected pressure set-point. The details of this system are described in this section. A schematic diagram showing the complex network of pressure measurement, control, and flow systems used in this work is shown in Figure 7.

The high degree of accuracy required for the main-chamber pressure measurement led to the selection of state-of-the-art, MKS 690A high accuracy Baratron pressure transducers (one of these is the red box in the foreground of Figure 6). These transducers have a stated accuracy of: 0.05% at full scale (FS), 0.06% of reading down to 10% of FS, and 0.1% of reading down to 1% FS. Two low-range (100 mTorr FS), two intermediate-range (1,000 mTorr FS), and one high-range (10,000 mTorr FS) pressure transducers are operated simultaneously to provide redundant measurements as a check of accuracy. Two Baratrons (a 100 mTorr and a 1,000 mTorr FS unit) are located near the pin-holes on the e-gun side of the test chamber, while the other three (a 100 mTorr, a 1,000 mTorr, and a 10,000 mTorr FS unit) are located on the diagnostic plate on the opposite side of the chamber. Tests show that redundant pairs of transducers typically agree to better than 0.5% of reading under actual test conditions, a good indication of overall accuracy. Some of this difference is undoubtedly real, as the pair of transducers located near the gas inlet typically show a slightly higher pressure that the similar unit mounted near the pin-hole outlet.

During testing, a flow of gas is admitted to the chamber to replace that pumped out through the e-gun pin-hole orifice. Chamber pressure is actively controlled by comparing the Baratron-measured pressure with an operator-selected pressure set-point; an MKS 244E pressure/flow controller maintains the desired pressure by regulating the flow into the chamber through an automated MKS 245 metal-seated proportioning control valve. Any of the five pressure transducers can be used by the controller, which allows operated-selected pressures to be maintained at set points anywhere from 1 mTorr to 10 Torr. Tests show that the flow controller provides exceptionally stable chamber pressures; for example, the system can maintain a pressure of 30.00 ± 0.01 mTorr over long periods of operation. Thus, the pressure measurement and flow-regulation subsystems provide the extremely accurate and precise control needed for this project.

5.5. Plate Assemblies

Significant thought was given to the design of the assemblies which hold the test plates (whose working surfaces are in contact with the gas and determine the gas/surface interface). One operational goal was that test plates could be interchanged in less than a day so that measurements with different materials/surfaces could be accomplished in a tractable length of time. Several additional, aggressive requirements are placed on the plate assemblies: 1) maintain a constant temperature across the test plate, 2) precisely position each plate surface independently, 3) maintain parallel alignment between the two plates, and 4) provide thermistor access for heat-flux measurements. The final design of the plate assembly does a very good job of meeting these requirements. A photograph of the plate assemblies in operation is shown in Figure 8 (*top*).

To provide interchangeability, the test plates are based on a 6-inch conflat flange that was reduced to a 14.27-cm OD. The experiments reported here use a 2.54-cm thick, 304 stainless steel conflat flange with a standard machined (lathe) surface (RMS roughness of a ~2 μm). In the future,

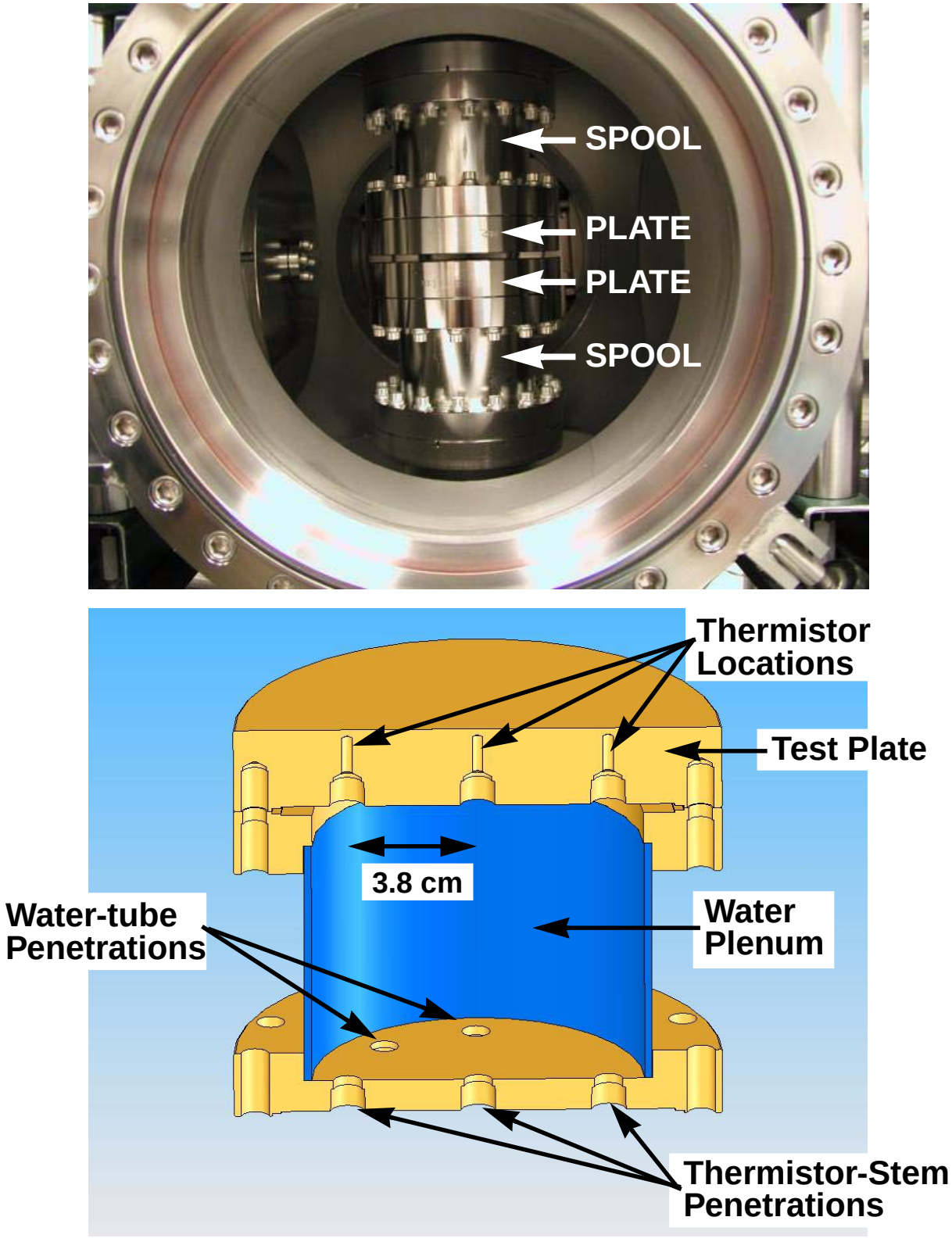

Figure 8. Plate assemblies. *Top:* photograph of plate assemblies looking through the observation window; *Bottom:* Schematic diagram of plate "spool" assembly.

additional surface conditions could be achieved by using different surface preparations for the stainless-steel plates, by using different plate materials, by coating a stainless-steel plate, or by bonding a new surface to an existing plate. The test plate is secured to a "spool" assembly, which is shown schematically in Figure 8 (*bottom*). The spool provides direct contact between a 0.62-liter plenum of water and the back-side of the test plate. Three high-precision Hart Scientific thermistors (stated accuracy 0.01°C) are embedded to within ~1.6 mm of the surface of each test plate: one thermistor is centered, while the other two are positioned at a radius of 1.5" (3.8 cm) as shown in Figure 8 (*bottom*). One thermistor is submerged within the water plenum of each spool. Hart thermistors are mounted on the tips of ~10-inch rigid stems, and penetrations for these stems are provided on the spool plate opposite the test-plate. The embedded thermistors are used to measure plate temperature and to check for uniformity, while the difference between the embedded thermistors and the submerged (bath) thermistor is used to infer heat flux (see below). A Hart Scientific calibration oil bath in conjunction with a standard reference thermistor was used to calibrate the test thermistors over an appropriate range of temperatures. All eight thermistors agreed to within 0.005°C, which is well within the manufacturers specifications. Our experience with these thermistors is that they are precise (repeatable) to better than 0.005°C in day-to-day operations. It is this extremely high degree of measurement precision that enables the accurate heat-flux measurements that are described below.

Two water baths (Neslab Model RTE-22) are used to control the temperature in the water plenum, which by direct contact controls the temperature of the test plates. The baths are marketed with a stated accuracy of 0.01°C but are stable to ~0.003°C. The water flows into each plenum through a 0.25-inch stainless-steel tube that is bent 90^{o} near its end and is directed towards the wall to promote mixing, as shown schematically in Figure 9. For the bottom plate assembly, the water exits through a tube placed in close proximity with the bottom of the test plate to inhibit bubble formation at the top of the water plenum (as shown in Figure 9). For the top plate assembly, the water exits through a tube flush-mounted in the spool-plate opposite of the test plate (not shown).

The spool assemblies are mounted to extension columns (see Figure 5) and extensible metal bellows that seal to the top and bottom flanges of the test chamber. The vertical position of each plate assembly is controlled by a separate precision positioner (Thermionics). These positioners can adjust the vertical position of the ~20-kg plate assemblies independently with ~10 micron accuracy. Software is used to control the position of each plate assembly independently, or the two positioners can be operated in a master/slave mode to maintain a fixed distance between the plates (so that the inter-plate gap can be scanned by the fixed electron beam).

5.6. Heat Flux Measurements

The plate assemblies were designed to allow temperature-difference measurements to be used to infer the axial heat flux between the two test plates. For this purpose, the temperature-difference of interest was between a central thermistor embedded just beneath the test-plate working surface and another immersed in the adjacent water plenum (see Figure 9). This is a challenging measurement strategy, as the heat flux through a low-pressure gas is known to be extremely small. The measurement is further complicated by the fact that the thermal conductivities of solids and liquids are very large compared to those of gases. Consequently, the expected temperature

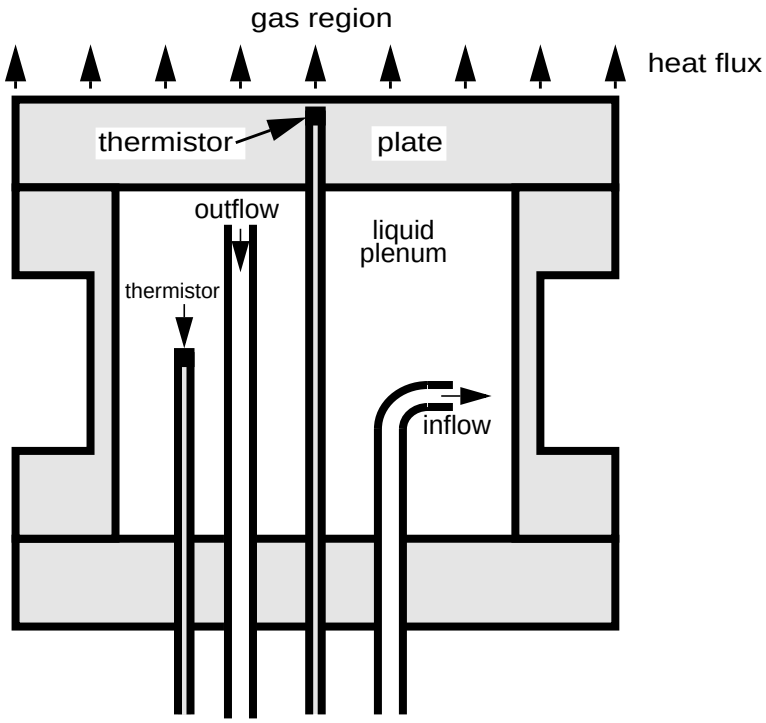

Figure 9. Elements of temperature-drop measurements in the “spool” assembly.

differences across the water plenum and stainless-steel plate were expected to be extremely small. To succeed, this measurement strategy requires that four critical assumptions be met: (1) that the expected small temperature drops can be accurately measured, (2) that radial heat flows (*e.g.*, parasitic heat losses) are small, (3) that a known heat flux can be identified to serve as a calibration point, and (4) that the measured temperature drop is linearly proportional to the axial heat flux between the bath and test-plate working surface.

It was originally believed that the thermal resistance across the water plenum would be small, based on the assumptions that the liquid volume was well mixed and thermally conductive. In this case, all of the temperature drop was expected to result from the thermal resistance of a ~2.5-cm thickness of 304 stainless steel. Early tests with the system provided an unexpected result: the measured temperature drops were found to be much larger than expected based on the thermal resistance of the stainless steel alone. An analysis of the thermal resistance of the combined water-plenum/steel plate system revealed a large temperature-drop contribution from the heat-transfer coefficient between the water plenum and the backside of the test plates (Torczynski *et al*., 2004). This fortuitous result, combined with the high precision of the Hart thermistors, allows precise temperature-drop measurements to be made even for the very low heat fluxes of interest.

As an example, Figure 10 shows measured temperature histories for nitrogen coupled with 304 stainless steel plates. The test was conducted with an inter-plate gap of 5 mm and the temperature baths set at 15°C and 35°C (approximately symmetric about room temperature). Thermistor readings were recorded with the chamber held near vacuum (left side of the plots) and for a series of pressures between 1 and 6700 mTorr (series of steps moving to the right side of the plots).

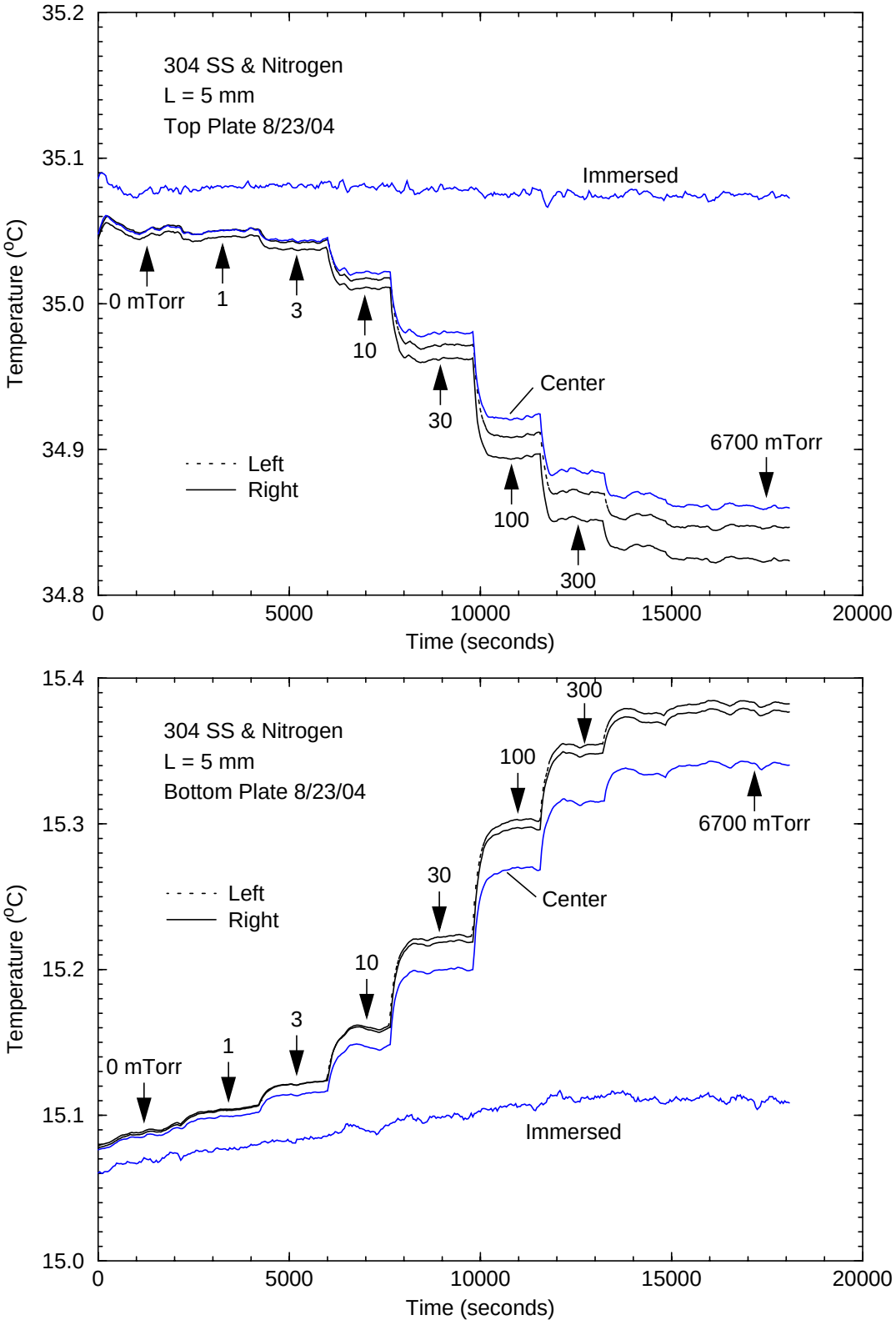

Figure 10. Temperature histories (nitrogen, 304 stainless steel, 5-mm gap).

Temperature histories are shown for both the top (hot) and bottom (cold) plates. The three embedded thermistors are labeled “center”, “left”, and “right”; the left and right thermistors are collinear with the central thermistor and symmetrically placed 3.8 cm radially outward from the centerline. The “immersed” thermistor is located in the central core of the water plenum. Note that, for each plate, the temperatures of the three embedded thermistors are always distinguishable from the immersed thermistor. It is the temperature differences between the embedded and immersed thermistors that are used to infer heat flux. These results clearly demonstrate that the present experimental apparatus is capable of measuring the small temperature differences needed in this study (satisfying assumption (1) from above).

Figure 10 suggests that temperature uniformity across each plate is good; the embedded thermistors at the center and sides differ by no more than ~0.05°C for all pressure conditions. The largest nonuniformities are encountered at the highest pressure (6700 mTorr), suggesting that parasitic heat losses (presumably from the sides of the test plates) are largest at high pressures. Differences between the left and right thermistors suggest that the temperature distribution across the plate becomes slightly asymmetric at high pressures as well although the largest observed asymmetry is typically less than ~0.02°C. Interestingly, the top (hot) plate shows stronger asymmetry than the bottom (cold) plate. These results demonstrate a high degree of temperature uniformity and symmetry across each plate, especially as the observed departures are small compared to the temperature difference between the test plates (typically 10-40°C). These observations provide support for assumption (2) made above.

The accurate determination of heat flux based on temperature measurements assumes that the temperature difference between the embedded and immersed thermistors is linearly proportional to the axial heat flux. Taking advantage of symmetry, we consider the difference between the temperatures of the central embedded thermistor, T_{center}, and the immersed thermistor, T_{im}. Temperature-difference histories for the data presented in Figure 10 are given in Figure 11, where the magnitude of the differences is $\left|T_{\text{center}} - T_{\text{im}}\right|$. One immediate observation is that the pressure steps are now much more clearly identifiable than in Figure 10. This improvement in signal is a result of the difference operation, which removes intermediate- and long-term drifts in the liquid-plenum temperature. Although these drifts are reasonably small (~0.05°C over 5 hours), they act to conceal the true trend of the temperature differences. For constant conditions (*e.g.*, fixed pressure, gap, plate temperatures), averaging the temperature-difference over time (30-60 minutes) significantly improves the signal-to-noise ratio of the measurements. Using time averaging, the current apparatus can resolve temperature-difference steps of as small as ~0.001°C. For example, when pressure is changed from 1 to 3 mTorr, the measured temperature difference increases by 0.009°C, about one order of magnitude larger than the minimum resolution (see Figure 11). Clearly, very small changes in heat flux can be resolved with the current system.

The next step in determining gas-phase conduction is to subtract parasitic heat losses which are present when the system is held near vacuum. In the absence of gas, any heat flux through the test plates must result from either radiation or solid conduction. For the present apparatus, it is believed that the majority of parasitic losses result from radiation. Thus, in the following discussion, parasitic losses observed under vacuum will be attributed to radiation. Radiation heat losses are clearly evident in Figure 11 for the 0 mTorr cases; for the top plate, this heat-loss contribution is labeled “RADIATION” in the figure and gives a temperature difference of

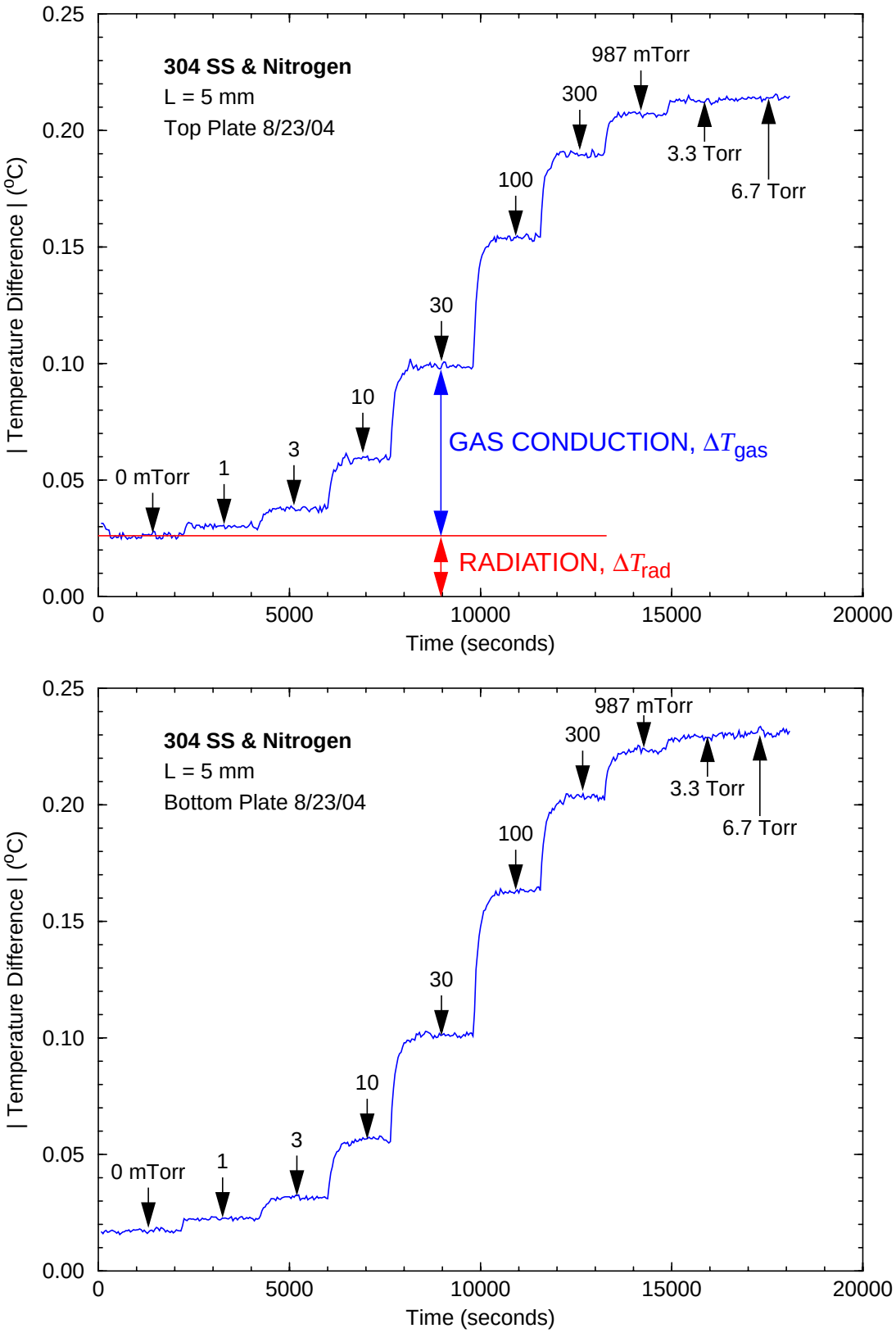

Figure 11. Temperature-difference histories (nitrogen, 304 stainless steel, 5-mm gap).

ΔT_{rad} = 0.026° C. The radiation loss for the cold plate is less, ΔT_{rad} = 0.017° C. The temperature-difference contribution from gas-phase conduction, ΔT_{gas}, is determined by subtracting the temperature difference observed under vacuum, ΔT_{rad}, from the total temperature difference:

$$\Delta T_{\text{gas}} = \Delta T - \Delta T_{\text{rad}}. \tag{24}$$

Although the radiation contribution is much smaller than gas-phase conduction at higher pressures, at pressures below a few mTorr radiation dominates.

The final step in determining heat flux from temperature-difference measurements is to establish a calibration point. One possibility is suggested by the high-pressure data of Figure 11, which clearly show that the measured temperature difference plateaus for pressures above ~5 Torr. The explanation for this behavior is that the continuum limit has been achieved, for which gas-phase heat conduction becomes independent of pressure (see Figure 4). The continuum heat flux, q_C, can be accurately calculated using Equation (7), the plate separation, and gas properties (see Chapter 3). Heat flux at arbitrary pressures can be determined by a simple scaling

$$\frac{q}{q_C} = \frac{\Delta T_{\text{gas}}}{\Delta T_C} \tag{25}$$

where

$$\Delta T_C = \lim_{P \to \infty} (\Delta T_{\text{gas}}) = \lim_{P \to \infty} (\Delta T - \Delta T_{\text{rad}}). \tag{26}$$

This strategy provides the calibration point needed to satisfy assumption (3) above.

The only remaining assumption, (4) from above, is that the heat flux through the test plate is linearly proportional to the measured temperature difference over the entire measurement range; this assumption is implicit in Equation (25). This assumption has not been proven yet although the consistency of the data presented in the next section suggest that this assumption is approximately valid. Additional discussion of this issue is presented in Chapter 6.

5.7. Electron Beam Fluorescence Measurements

Precision measurement of the gas density (or temperature) gradient between two opposing parallel plates held at different temperatures represents a very challenging application for electron beam fluorescence methods. Consider the case of two plates held at 278 K and 318 K, respectively. The maximum expected variation in gas density between the cold and hot surfaces is approximately 14%. In practice, however, the measurable range is likely to be significantly lower. Due to pressure constraints for proper e-gun operation and pumping limitations, the upper limit in operating pressure in the test chamber is a few tens of mTorr when the e-beam diagnostic is used. Also, the ionization cross sections in typical gases are sufficiently high that substantial attenuation

of the electron beam intensity occurs at higher pressures. Under such rarefied conditions, temperature jumps at the walls significantly reduce gas density gradients. For example, DSMC calculations suggest that the density gradient is reduced by about 50% for 20 mTorr argon with a 1-cm plate separation, so that the total expected density variation is only ~7%. To establish the gas density profile between the two plates with sufficient accuracy, data within the 7% range need to be accurate to a few percent. Hence, it is desirable to establish fluorescence intensities (thereby inferring gas densities and temperatures) to within 0.5% or better. Earlier electron beam studies in the parallel plate geometry have not approached this level of accuracy (Teagan and Springer, 1968; Alofs *et al.*, 1971).

Our current design for electron beam fluorescence measurements is illustrated schematically in Figure 12. The e-beam-induced fluorescence intensity is measured at a location near the axial centerline of the two parallel plates. Light generated in this region is collected by a 5-inch-diameter, 7-inch-focal-length lens. This lens is mounted just outside the principal optical port of the main vacuum chamber (*cf.* Figure 12). The light is routed through an optical chopper and refocused onto the input face of a photomultiplier tube (PMT). A rectangular iris is placed in the beam path to exclude light generated outside the region of interest. The resulting PMT signal is processed by an Oriel Corporation Merlin^{TM} Radiometer. This system utilizes the optical chopper to discriminate against stray light.

To map out the gas density variation between the two plates, it is necessary to probe the fluorescence intensity at various distances above the bottom plate. For these measurements, the electron beam location and plate separations are held fixed while the precision translators are used to move the plates in tandem. With this approach, gas density variations can be monitored at increments of 0.5 mm or smaller. Signals are averaged and recorded at each location using the TRACQ32^{TM} software package supplied by Spectra-Physics Lasers and Photonics. For density measurements in argon, we utilized a narrowband interference filter (10-nm bandpass, full-width at half-maximum) to isolate the relatively intense 461.0-nm line. This line has been identified as particularly well-suited to the purposes of fluorescence probing (negligible collisional quenching, minimal secondary excitation halos, etc. (Gochberg, 1997)). Fairly precise measurements of 461.0-nm argon fluorescence have been obtained with this diagnostic setup. Measured in output voltage, typical averaged signal intensities are ~10 μV with a standard deviation of 40-50 nV. These specifications are consistent with the requirements outlined above. Currently, the principal source of uncertainty in the fluorescence measurements appears to arise from long-term drift in the electron beam current. To characterize this drift, we intend to install a fluorescence monitor that views a region at essentially constant gas pressure (*e.g.*, near the input pinhole in the main chamber).

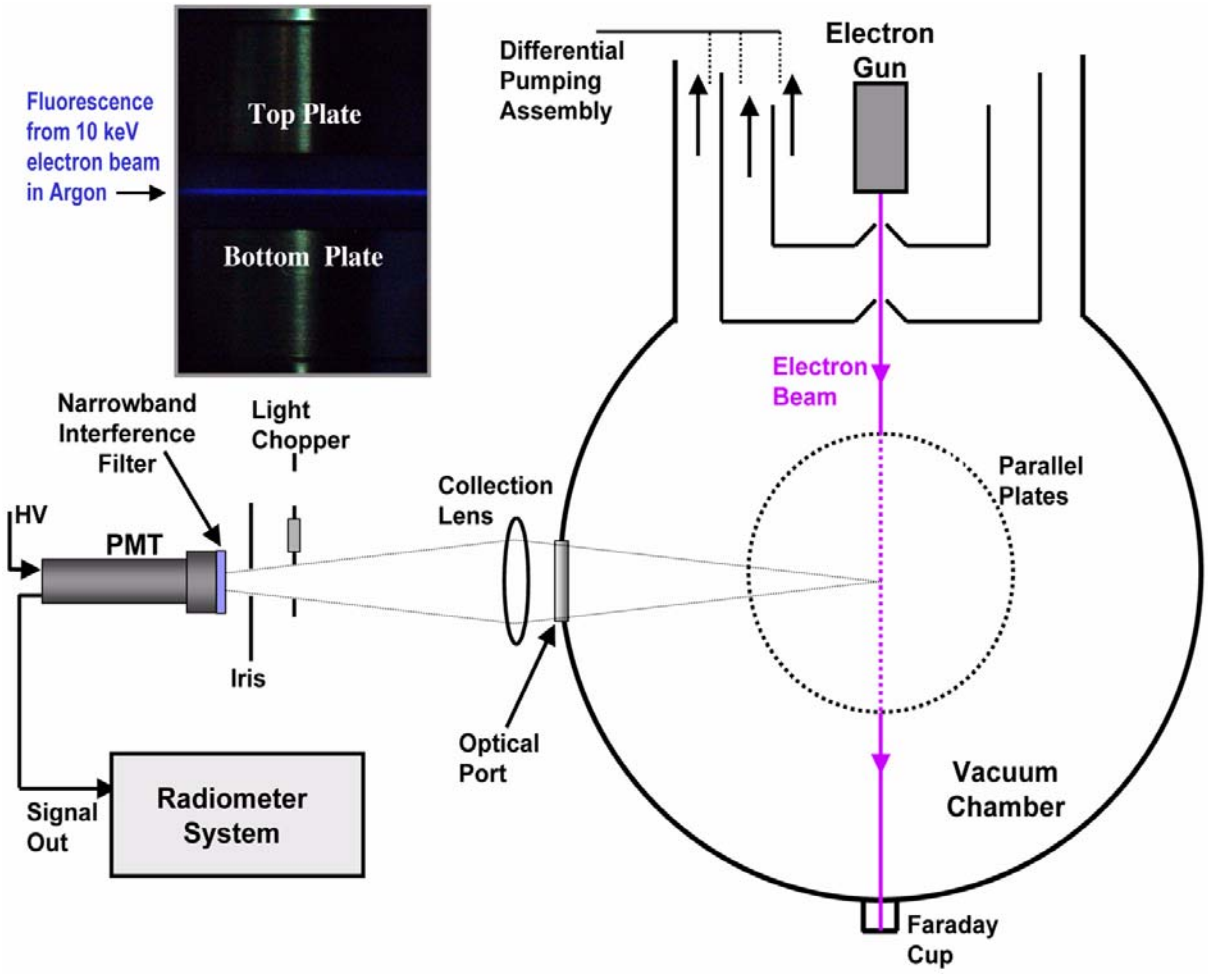

Figure 12. Schematic diagram of electron-beam fluourescence diagnostic.

6. Experimental Results

6.1. Overview

This chapter presents data from selected tests that highlight the present capabilities of the test chamber and associated diagnostics. The dependence of measured temperature differences (between embedded and immersed thermistors) on pressure is used to infer the dependence of heat flux on pressure; from these data, thermal accommodation coefficients can be extracted. Thermal accommodation coefficients are determined in this way for helium, argon, and nitrogen coupled with machined 304 stainless steel plates. Results are presented for several combinations of plate temperatures and inter-plate gaps. Several gas-density profiles measured by electron-beam fluorescence are given for argon at pressures where large temperature jumps are expected.

6.2. Helium Heat-Flux and Accommodation Measurements

Figure 13 shows cold-plate, temperature-difference time histories for helium gas coupled with 304 stainless steel plates separated by a 10-mm gap and with $T_c = 20.1°\mathrm{C}$ and $T_h = 30.1°\mathrm{C}$. The clearly distinguishable steps correspond to measurements at a series of test pressures from vacuum to 10 Torr. The top plot shows the entire time profile, while the bottom plot shows an expanded vertical scale to clarify the behavior at low pressures. Gas-phase conduction is clearly distinguishable from radiation (the temperature difference observed under vacuum conditions) for pressures higher than a few mTorr. At higher pressures, the measured temperature differences are remarkably constant at each pressure step.

The temperature-difference data presented in Figure 13 can be used to infer heat flux and thermal accommodation in the following manner. The analysis begins with the Sherman-Lees interpolation formula, rewritten in the form of Equation (18), which is repeated here:

$$\frac{1}{q} = \frac{1}{q_C} + \frac{1}{q_C} \cdot \frac{2KT}{L\left(\frac{\alpha}{2-\alpha}\right)\left(1+\frac{\zeta}{4}\right)\bar{c}} \cdot \frac{1}{P}.$$

From Chapter 5, a relationship between heat flux and measured temperature differences was postulated in Equation (25) which is repeated here as well:

$$\frac{q}{q_C} = \frac{\Delta T_{\mathrm{gas}}(P)}{\Delta T_C}$$

where $\Delta T_{\mathrm{gas}}(P) = \Delta T(P) - \Delta T_{\mathrm{rad}}$, $\Delta T(P)$ is the time-averaged temperature difference measured at pressure *P*, ΔT_{rad} is the time-averaged temperature difference from radiation, and ΔT_C is the temperature difference that would be observed in the continuum limit (*i.e.*, in the limit

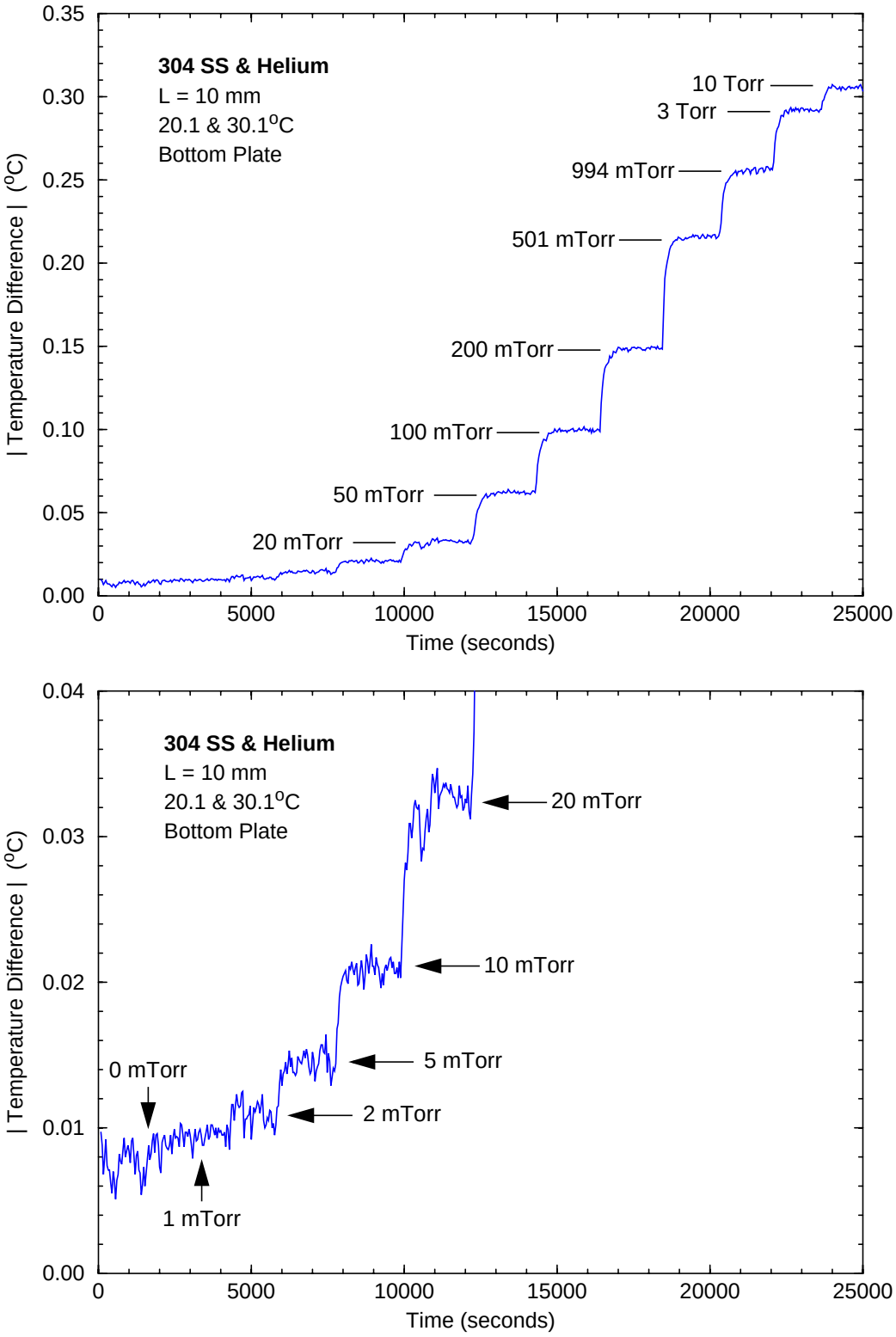

Figure 13. Temperature-difference histories for bottom plate (helium, T_c=20.1°C, T_h=30.1°C, 304 stainless steel, 10-mm gap).

of infinite pressure). Combining these two results gives an expression for the pressure-dependence of ΔT_{gas}:

$$\frac{1}{\Delta T_{\text{gas}}} = \frac{1}{\Delta T_C} + \frac{1}{\Delta T_C} \cdot \frac{2KT}{L\left(\frac{\alpha}{2-\alpha}\right)\left(1+\frac{\zeta}{4}\right)\bar{c}} \cdot \frac{1}{P}. \tag{27}$$

Equation (27) is not rigorous, being based on two assumptions: 1) that the Sherman-Lees interpolation formula correctly describes the pressure-dependence of gas heat flux, and 2) that the measured temperature differences are linearly related to the axial heat flux. Thus, Equation (27) is proposed as a means of correlating the experimental measurements. The form of Equation (27) suggests that a plot of $1/\Delta T_{\text{gas}}$ against inverse pressure, $1/P$, should be linear. A graphical interpretation of such a plot is that the *y*-axis intercept equals the reciprocal of the continuum-limit temperature difference, ΔT_C, and that the slope is a function of known quantities except for the accommodation coefficient.

The helium/stainless steel data from Figure 13 have been analyzed in the manner described above and plotted in the form suggested by Equation (27) in the temperature-jump regime ($\text{Kn} < 0.1$). Data in the pressure range $200 < P < 10,000$ mTorr ($26.66 < P < 1333.2$ Pa) were considered, for which $\text{Kn} < 0.073$. The results are plotted in Figure 14 for the bottom (cold) and top (hot) plates. The linear nature of the data when plotted in this fashion is clearly evident. Linear regressions to the data from each plate give correlation coefficients near unity, $r^2 = 0.9999$: the reciprocal of the intercept and the slope are given in Table (3). The reciprocal of the regression intercepts give continuum-limit temperature differences of $\Delta T_C = 0.3057$ and 0.2832°C for the cold and hot plates, respectively. Inspection of the bottom-plate temperature histories plotted in Figure 12 reveals that the 10-Torr measurement has reached only about 97% of the continuum limit. Note that the total temperature difference is plotted in Figure 12 so that the radiation contribution should be included, *i.e.* $\Delta T = \Delta T_C + \Delta T_{\text{rad}} = 0.3507 + 0.0080 = 0.3587°\text{C}$.

The regression slopes can be used to determine the thermal accommodation coefficient according to Equation (27). The resulting values for the cold and hot plate, $\alpha = 0.381$ and 0.378, respectively, are in excellent agreement. This is a satisfying result, as the heat flux between the two plates should be exactly equal in the ideal one-dimensional situation where parasitic heat losses and nonlinearities can be neglected. The determination of thermal accommodation for gas/surface interactions is the goal of this experiment. The results reported here are consistent with a Maxwell wall model in which 38% of helium molecules undergo a diffuse, thermally-accommodated reflection, while the remainder undergo a specular reflection. Moreover, the good agreement between data and regression in Figure 14 suggest that the Sherman-Lees interpolation function works exceptionally well in the temperature jump regime.

A similar test as above was repeated with the same conditions except for a 40°C temperature difference between the plates: helium/stainless steel, 10-mm gap, $T_c = 5.2°\text{C}$ and $T_h = 45.0°\text{C}$. The temperature-history profiles showed the same qualitative behavior as Figure 13, except that the temperature differences were multiplied by approximately a factor of four. The data are analyzed in the manner described above and plotted in the pressure range

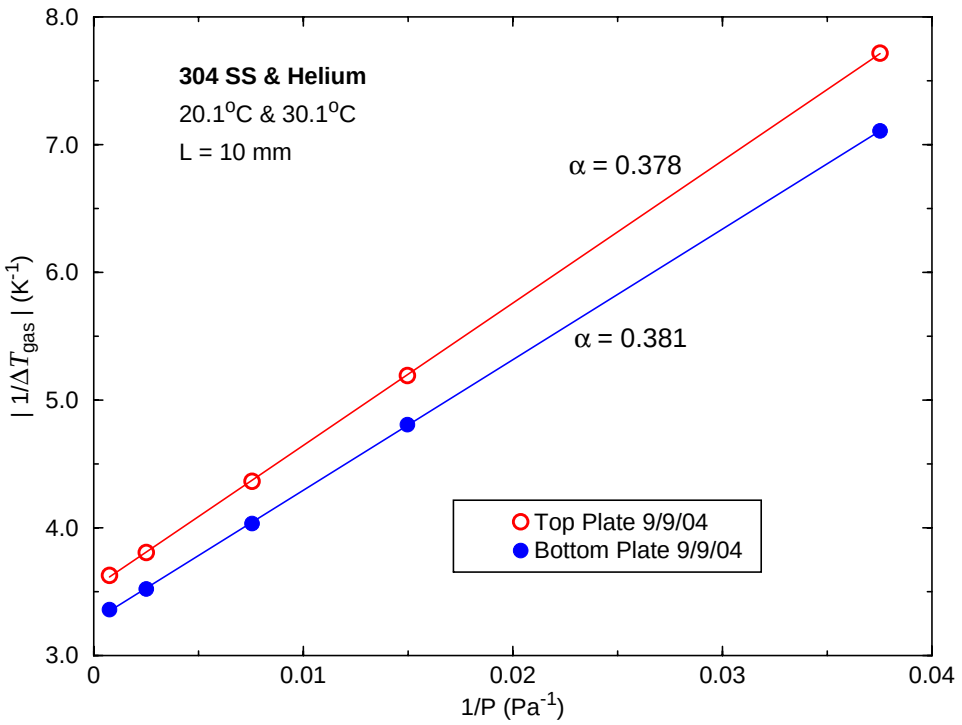

Figure 14. Plot of inverse ΔT_{gas} vs. inverse pressure in the temperature-jump regime (helium, T_c=20.1°C, T_h=30.1°C, 304 stainless steel, 10-mm gap).

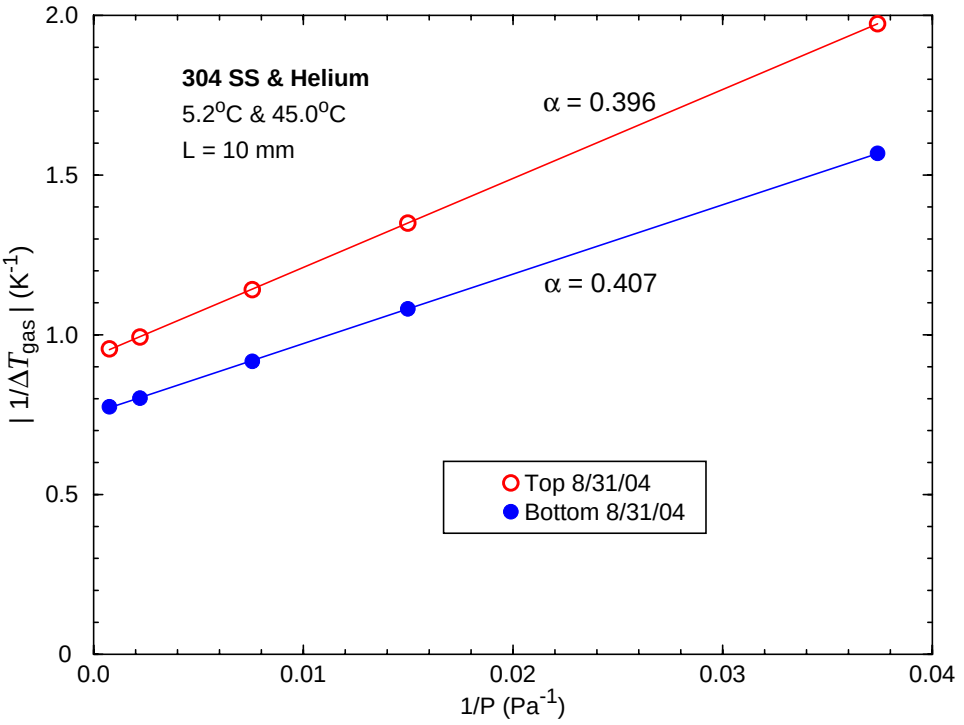

Figure 15. Plot of inverse ΔT_{gas} vs. inverse pressure in the temperature-jump regime (helium, T_c=5.2°C, T_h=45.0°C, 304 stainless steel, 10-mm gap).

$200 < P < 10,000$ mTorr ($26.66 < P < 1333.2$ Pa). The results are plotted in Figure 15 for the bottom (cold) and top (hot) plates. As before, the linear nature of the data when plotted in this fashion is clearly evident. The accommodation coefficients calculated for the cold and hot plates, $\alpha = 0.407$ and 0.396, respectively, are in good agreement; however, the difference between the two is slightly larger than with the previous run. The average accommodation for the 40°C case, $\alpha = 0.401$, is also slightly higher than for the 10°C case, $\alpha = 0.380$.

The slightly different accommodations observed for these two test cases could be either real (*i.e.*, resulting from a temperature-dependent accommodation) or an artifact resulting from nonideal behavior of the system (*i.e.*, a nonlinear relationship between ΔT_{gas} and the actual heat flux). Additional experimental studies are planned to investigate these possibilities. In any case, the accommodation coefficients measured under two different temperature gradients differ by only 0.02, which is taken as an estimate of our uncertainty. The accommodation coefficient resulting from the lower-gradient test is preferred, as in this case the two estimates for α are in better agreement and as the two plates are closer in temperature. Based on these two tests, the best value for the thermal accommodation coefficient for helium coupled with 304 stainless steel is $\alpha = 0.38 \pm 0.02$.

6.3. Argon and Nitrogen Heat-Flux and Accommodation Measurements

Tests like those reported above for helium were also conducted with argon and nitrogen coupled with 304 stainless steel plates. The plate separation was 10 mm and the plate temperatures were held at $T_c = 5.2°\text{C}$ and $T_h = 45.0°\text{C}$. The same test procedure was used, namely to systematically change the chamber pressure and record temperature-difference histories. Data in the temperature-jump regime ($\text{Kn} < 0.1$) were analyzed in the manner described above and plotted in the form suggested by Equation (27). The pressure range over which the data were analyzed was $100 < P < 10,000$ mTorr ($13.3 < P < 1333$ Pa), for which $\text{Kn} < 0.05$.

The results are given in Figure 16 for the argon (*top*) and nitrogen (*bottom*). As with helium, the linear nature of the data when plotted in this fashion is clearly evident. For argon, the accommodation coefficients calculated for the cold and hot plates, $\alpha = 0.890$ and 0.883, respectively, are in very good agreement. For nitrogen, the accommodation coefficients calculated for the cold and hot plates, $\alpha = 0.825$ and 0.782, respectively, are in fair agreement. As mentioned above, analyses of the two plates should give exactly the same value for accommodation as they are ideally experiencing the same heat flux (neglecting parasitic heat losses and system nonlinearities). The nitrogen test presented in Figure 16 shows the largest difference in cold- and hot-plate accommodation values that have been observed in the present study. One possible explanation was that the temperature histories for this nitrogen data set showed more noise than the other data sets presented. In any case, the two values for the accommodation coefficient differ from their mean by only ± 0.02.

Based on analysis of these two tests, the best values for the thermal accommodation coefficient for argon and nitrogen coupled with 304 stainless steel are $\alpha = 0.88 \pm 0.02$ and $\alpha = 0.80 \pm 0.02$, respectively. Unlike helium, these heavier gases show near unity accommodation; this result is consistent with theoretical expectations.

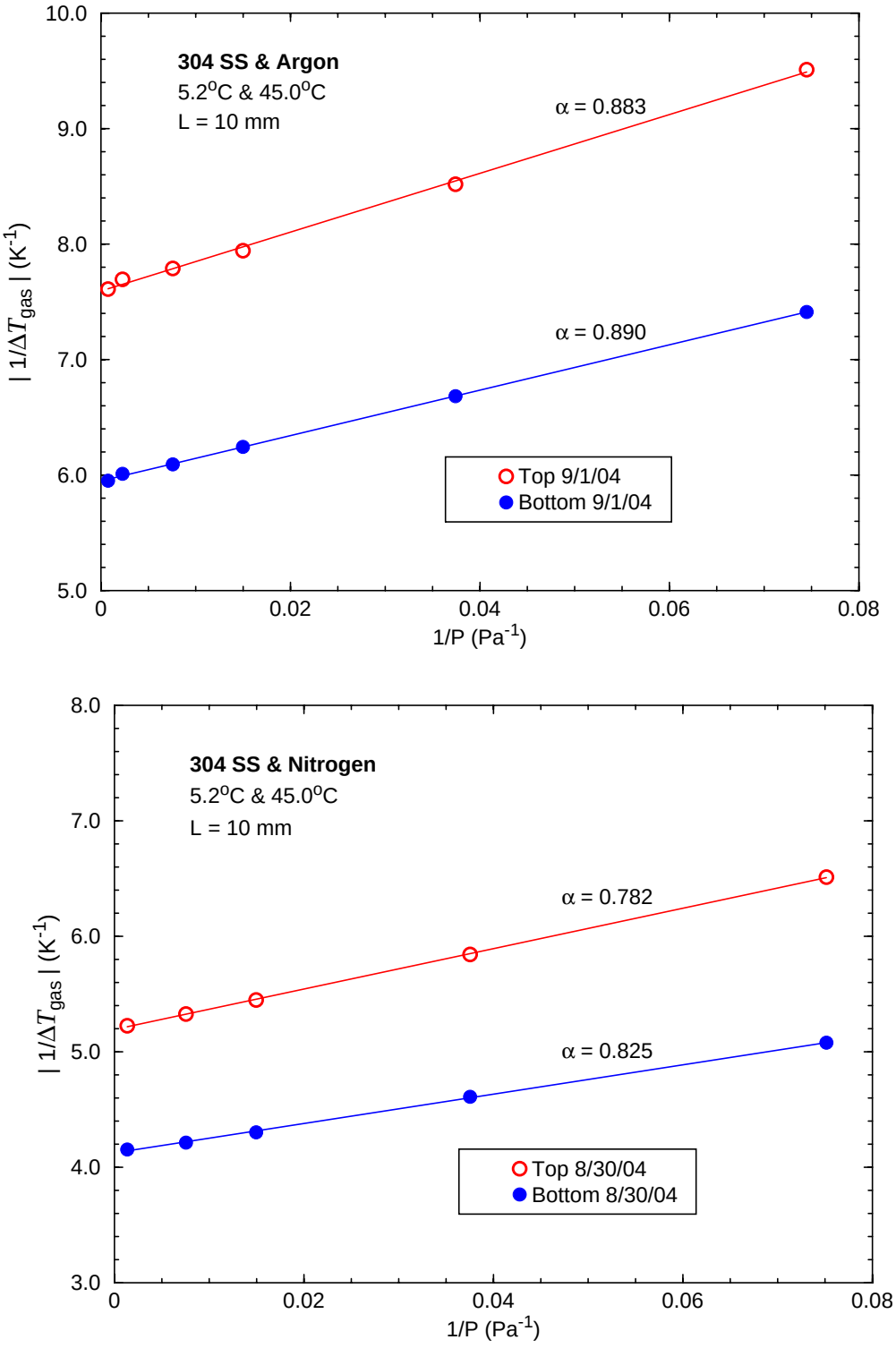

Figure 16. Plot of inverse ΔT_{gas} vs. inverse pressure in the temperature-jump regime. *Top:* argon, T_c=5.2°C, T_h=45.0°C, 304 stainless steel, 10-mm gap. *Bottom:* nitrogen, T_c=5.2°C, T_h=45.0°C, 304 stainless steel, 10-mm gap.

6.4. Summary of Heat-Flux and Accommodation Measurements

Table 3. Gas/Stainless Steel Summaries

Gas, L, T_c/T_h	Bottom Plate			Top Plate		
	ΔT_C (K)	slope (Pa/K)	α	ΔT_C (K)	slope (Pa/K)	α
Helium, 10 mm 20.1/30.1°C	0.3057	102.23	0.381	0.2832	111.43	0.378
Helium, 10 mm 5.2/45.0°C	1.324	21.725	0.407	1.0723	27.823	0.396
Argon, 10 mm, 5.2/45.0°C	0.1680	19.644	0.890	0.1317	25.419	0.883
Nitrogen, 10 mm, 5.2/45.1°C	0.2425	12.725	0.825	0.1925	17.519	0.782

6.5. Electron Beam Fluorescence Measurements

As discussed in Section 5.7, the use of e-beam fluorescence to make highly-accurate density-profile measurements for small temperature gradients in a low-pressure gas is challenging. The difficulty of the task is further increased by a variety of optical (*e.g.*, geometric clipping of scattered fluorescence light by plates) and physical challenges (*e.g.*, long-term drift in the e-beam current). Consequently, the accuracy of gas-density profiles is not yet as high as we desire. We continue to work to improve the accuracy of our e-beam fluorescence measurements.

Several measured gas-density profiles are shown in Figure 17 to demonstrate our current level of expertise using e-beam fluorescence. Both profiles were taken with argon coupled with 304 stainless steel machined plates at a system pressure of 20 mTorr. Gas density at each position was inferred from the measured fluorescence intensity normalized by the fluorescence intensity mid-way between the plates. The axial position of the measurement was changed by translating the test plates in tandem about the fixed e-beam position. The ideal gas law was used to convert the normalized density data into a temperature profile. The measured profiles clearly show the flattening of the temperature gradient resulting from near-wall temperature jumps. Scatter in the data contributes to the non-monotonic appearance of the data.

DSMC simulations of the experimental conditions were performed for comparison. The calculations assumed a Maxwell wall model and a thermal accommodation of $\alpha = 0.9$ (close to the experimental value of 0.88 from the previous section). The calculations are in qualitative agreement with the data although some systematic departures are evident. Given the uncertainty in the data, it is difficult to say if the observed differences are significant.

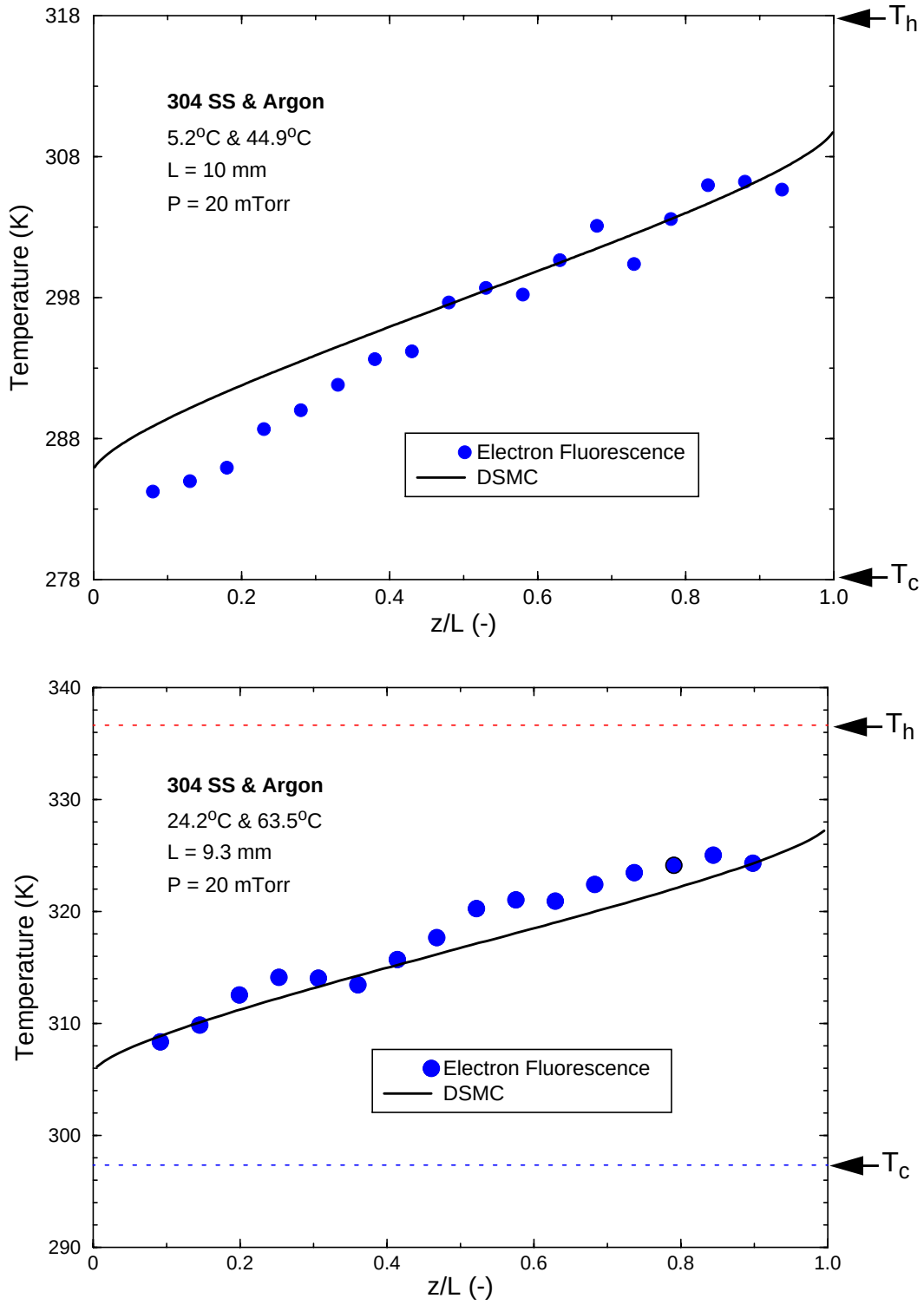

Figure 17. Temperature profiles from e-beam fluorescence intensity measurements.
Top: 20 mTorr argon, T_c=5.2°C, T_h=44.9°C, 304 stainless steel, 10-mm gap.
Bottom: 20 mTorr argon, T_c=24.2°C, T_h=63.5°C, 304 stainless steel, 9.3-mm gap.

7. Conclusions

Heat transfer to surfaces immersed in noncontinuum (transitional or rarefied) gas flow continues to be an active area of research. Gases exhibit noncontinuum effects when the characteristic length scale of the system becomes comparable to the gas mean free path. Thus, these effects become important when either the system length scale becomes small (*e.g.*, Micro Electro Mechanical Systems) or when the gas pressure becomes low (*e.g.*, semiconductor manufacturing or Extreme Ultra Violet Lithography). *A priori* prediction of noncontinuum, gas-phase heat flux requires a detailed description of the gas-surface interaction. Unfortunately, and despite considerable effort over the past century, reliable gas-surface interaction mechanisms are still lacking. This gap in our understanding becomes increasingly serious as modelers are asked to perform ever more sophisticated engineering analyses of systems exhibiting marked noncontinuum behavior. It is well recognized that the remedy to this dilemma lies in the development of a reliable, experimentally-validated database of gas-surface interaction models. Ideally, this database would span the wide range of gas-surface combinations that are of interest in modern engineering applications. This LDRD-funded study has taken a major step toward meeting this need by developing an experimental facility that can provide the needed data.

Under this LDRD, we have built and demonstrated an experimental facility that can be used to determine thermal accommodation coefficients from measured inter-plate gas-density profiles and from the pressure-dependence of heat flux between two parallel plates. Measurements of gas density profiles and heat flux can now be made under identical conditions, eliminating an important limitation of earlier studies. The application of electron-beam fluorescence to measure gas density profiles is demonstrated, although additional work is needed to improve the accuracy of the data. Heat flux between the plates is inferred from temperature-drop measurements. The use of high-precision thermistors and the careful control of experimental conditions allow the heat-flux measurements to be made with great precision.

The system can be operated with a variety of gases (monatomic, diatomic, polyatomic, mixtures) and carefully controlled, well-characterized surfaces of different types (metals, ceramics) and conditions (smooth, rough). The measurements reported here are for 304 stainless steel plates with a standard milled surface coupled with argon, helium, and nitrogen. The resulting heat-flux and gas-density-profile data are analyzed using analytic and computational models to determine whether a simple Maxwell gas-surface interaction model is adequate to represent all of the observations. Based on this analysis, thermal accommodation coefficients for 304 stainless steel coupled with argon, nitrogen, and helium are determined to be 0.88, 0.80, and 0.38, respectively, with an estimated uncertainty of ± 0.02.

References

Alofs, D. J., Glagan, R. C., and Springer, G. S. (1971) “Density distribution measurements in rarefied gases contained between parallel plates at high temperature differences,” *Physics of Fluids* **14**: 529-533.

Arkilic, E. B., Breuer, K. S., and Schmidt, M. A. (2001) “Mass flow and tangential momentum accommodation in silicon micromachined channels,” *Journal of Fluid Mechanics* **437**: 29-43.

Aziz, R. A., Janzen, A. R., and Moldover, M. R. (1995) “*Ab initio* calculations for helium: a standard for transport property measurements,” *Physical Review Letters* **74**(9): 1586-1589.

Bich, E., Millat, J., and Vogel, E. (1990) “The viscosity and thermal conductivity of pure monatomic gases from their normal boiling point up to 5000 K in the limit of zero density and at 0.101325 MPa,” *Journal of Physical and Chemical Reference Data* **19**(6): 1289-1305.

Bird, G. A. (1970) “Direct simulation and the Boltzmann equation,” *Physics of Fluids* **13**: 2676-2681.

Bird, G. A. (1976) *Molecular Gas Dynamics*, Clarendon Press, Oxford, UK.

Bird, G. A. (1978) “Monte Carlo simulation of gas flows,” *Annual Review of Fluid Mechanics* **10**: 11-31.

Bird, G. A. (1994) *Molecular Gas Dynamics and the Direct Simulation of Gas Flows*, Clarendon Press, Oxford, UK.

Chapman, S., and Cowling, T. G. (1970) *The Mathematical Theory of Non-Uniform Gases*, third edition, Cambridge University Press, Cambridge, UK.

Gallis, M. A., Torczynski, J. R., and Rader, D. J. (2004) “Molecular gas dynamics observations of Chapman-Enskog behavior and departures therefrom in nonequilibrium gases,” *Physical Review E* **69**, paper 042201.

Gochberg, L. A. (1997) “Electron beam fluorescence methods in hypersonic aerothermodynamics,” *Progress in Aerospace Science* **33**: 431-480.

Gombosi, T. I. (1994) *Gaskinetic Theory*, Cambridge University Press, Cambridge, UK.

Hurly, J. J., and Moldover, M. R. (2000) “*Ab initio* values of the thermophysical properties of helium as standards,” *Journal of the Research of the National Institute of Standards and Technology* **105**(5): 667-688.

Karniadakis, G. E., and Beskok, A. (2002) *Micro Flows: Fundamentals and Simulations*, Springer-Verlag, New York, NY.

Kennard, E. H. (1938) *Kinetic Theory of Gases*, McGraw-Hill, New York, New York.

Klebanoff, L. E., and Rader, D. J. (2000) "Protection of lithographic components from particle contamination," U.S. Patent #6,153,044, issued November 28.

Liu, C. Y., and Lees, L. (1961) "Kinetic theory description of plane compressible Couette flow," in *Rarefied Gas Dynamics*, L. Talbot, ed., Academic Press, New York, pp. 391-428.

Maxwell, J. C. (1890) *The Scientific Papers of James Clark Maxwell*, Vol. 2, Cambridge University Press, London and New York.

Ohwada, T. (1996) "Heat flow and temperature and density distributions in a rarefied gas between parallel plates with different temperatures," *Physics of Fluids* **8:** 2153-2160.

Rader, D. J., Dedrick, D. E., Beyer, E. W., Leung, A. H., and Klebanoff, L. E. (2002) "Verification studies of thermophoretic protection for EUV masks," in Emerging Lithographic Technologies VI, Roxanne L. Engelstad, ed., *Proceedings of the SPIE* **4688**: 182-193.

Saxena, S. C., and Joshi, R. K. (1989) *Thermal Accommodation and Adsorption Coefficients of Gases*, New York, Hemisphere Publishing Corporation.

Schaaf, S. A., and Chambre, P. L. (1958) "Flow of rarefied gases," in *Fundamental of Gasdynamics*, H. W. Emmons, ed., Vol. III, Princeton University Press, Princeton, NJ, pp. 687-739.

Sherman, F. S. (1963) "A survey of experimental results and methods for the transition regime of rarefied gas dynamics," in *Rarefied Gas Dynamics* Vol. II, J. A. Lauermann, ed., Academic Press, New York, pp. 228-260.

Sniegowski, J. J., and de Boer, M. P. (2000) "IC-compatible polysilicon surface micromachining," *Annual Reviews of Material Science* **30**: 299-333.

Springer, G. S. (1971) "Heat transfer in rarefied gases," in *Advances in Heat Transfer*, T. F. Irvine and J. P. Hartnett, eds., Academic Press, New York, pp. 163-218.

Stephan, K., Krauss, R., and Laesecke, A. (1987) "Viscosity and thermal conductivity of nitrogen for a wide range of fluid states," *Journal of Physical and Chemical Reference Data* **16**(4): 993-1023.

Teagan, W. P. and Springer, G. S. (1968) "Heat-transfer and density-distribution measurements between parallel plates in the transition regime," *Physics of Fluids* **11**: 497-506.

Torczynski, J. R., Gallis, M. A., and Rader, D. J. (2003) "Using DSMC to compute the force on a particle in a rarefied gas flow," in *Rarefied Gas Dynamics: 23rd International Symposium*, A. D. Ketsdever and E. P. Muntz, eds., American Institute of Physics, Melville, NY.

Torczynski, J. R., Trott, W. M., Rader, D. J., and Gallis, M. A. (2004) “Sensitivity enhancement of rarefied-gas heat-flux measurements,” Internal Memorandum, Sandia National Laboratories, Albuquerque, NM, dated April 7.

Wadsworth, D. C. (1993) “Slip effects in a confined rarefied gas: I: Temperature slip,” *Physics of Fluids A* **5**: 1831-1839

Wagner, W. (1992) “A convergence proof for Bird’s Direct Simulation Monte Carlo Method for the Boltzmann equation,” *Journal of Statistical Physics* **66**: 1011-1044.

Yang, H., and Bennett, T. D. (2000) “Time of flight measurements of thermal accommodation coefficient,” *Proceedings of the 34th National Heat Transfer Conference*, Pittsburg, PA, August 20-22, Paper NHTC2000-12035.

Distribution

1	MS 0841	Org. 9100	C.	W.	Peterson (acting)
1	MS 0824	Org. 9110	W.	L.	Hermina
1	MS 0834	Org. 9112	J.	E.	Johannes
1	MS 0834	Org. 9112	C.	J.	Bourdon
1	MS 0834	Org. 9112	J.	N.	Castañeda
1	MS 0834	Org. 9112	T.	W.	Grasser
1	MS 0834	Org. 9112	S.	P.	Kearney
1	MS 0834	Org. 9112	L.	M.	Phinney
5	MS 0834	Org. 9112	D.	J.	Rader
5	MS 0834	Org. 9112	W.	M.	Trott
1	MS 0826	Org. 9113	S.	N.	Kempka
3	MS 0826	Org. 9113	M.	A.	Gallis
1	MS 0826	Org. 9113	E.	S.	Piekos
3	MS 0826	Org. 9113	J.	R.	Torczynski
1	MS 0826	Org. 9113	C.	C.	Wong
1	MS 0834	Org. 9114	J.	S.	Lash
1	MS 0836	Org. 9117	R.	O.	Griffith
1	MS 0836	Org. 9117	R.	J.	Buss
1	MS 0123	Org. 1011	D.	L.	Chavez (LDRD Office)
1	MS 0521	Org. 2520	M.	R.	Prairie
1	MS 0151	Org. 9750	A.	C.	Ratzel
1	MS 9018	Org. 8945-1	Central Technical Files		
2	MS 0899	Org. 9616	Technical Library		